Chemical Science

ROYAL SOCIETY OF CHEMISTRY

EDGE ARTICLE

View Article Online
View Journal | View Issue



Cite this: *Chem. Sci.*, 2020, **11**, 3936

All publication charges for this article have been paid for by the Royal Society of Chemistry



# Trends in trigonal prismatic Ln-[1]ferrocenophane complexes and discovery of a $Ho^{3+}$ single-molecule magnet†

Trevor P. Latendresse,[a] Veacheslav Vieru,[bc] Apoorva Upadhyay,[ad] Nattamai S. Bhuvanesh,[a] Liviu F. Chibotaru*[b] and Michael Nippe*[a]

Lanthanide metallocenophanes are an intriguing class of organometallic complexes that feature rare six-coordinate trigonal prismatic coordination environments of 4f elements with close intramolecular proximity to transition metal ions. Herein, we present a systematic study of the structural and magnetic properties of the ferrocenophanes, $[LnFc_3(THF)_2Li_2]^-$, of the late trivalent lanthanide ions (Ln = Gd (**1**), Ho (**2**), Er (**3**), Tm (**4**), Yb (**5**), Lu (**6**)). One major structural trend within this class of complexes is the increasing diferrocenyl ($Fc^{2-}$) average twist angle with decreasing ionic radius ($r_{ion}$) of the central Ln ion, resulting in the largest average $Fc^{2-}$ twist angles for the $Lu^{3+}$ compound **6**. Such high sensitivity of the twist angle to changes in $r_{ion}$ is unique to the here presented ferrocenophane complexes and likely due to the large trigonal plane separation enforced by the ligand (>3.2 Å). This geometry also allows the non-Kramers ion $Ho^{3+}$ to exhibit slow magnetic relaxation in the absence of applied dc fields, rendering compound **2** a rare example of a Ho-based single-molecule magnet (SMM) with barriers to magnetization reversal ($U$) of 110–131 $cm^{-1}$. In contrast, compounds featuring Ln ions with prolate electron density (**3**–**5**) don't show slow magnetization dynamics under the same conditions. The observed trends in magnetic properties of **2**–**5** are supported by state-of-the-art *ab initio* calculations. Finally, the magneto-structural relationship of the trigonal prismatic Ho-[1]ferrocenophane motif was further investigated by axial ligand (THF in **2**) exchange to yield $[HoFc_3(THF^*)_2Li_2]^-$ (**2-THF***) and $[HoFc_3(py)_2Li_2]^-$ (**2-py**) motifs. We find that larger average $Fc^{2-}$ twist angles (in **2-THF*** and **2-py** as compared to in **2**) result in faster magnetic relaxation times at a given temperature.

Received 27th February 2020
Accepted 23rd March 2020

DOI: 10.1039/d0sc01197e

rsc.li/chemical-science

## Introduction

Single-molecule magnets (SMMs) are discrete molecules having a bistable magnetic ground state and a sufficient energy barrier to magnetization reversal ($U$) which can lead to magnetic hysteresis of purely molecular origin.[1] SMMs represent the smallest magnetic units that can be predictively modified with synthetic chemistry. This renders SMMs highly attractive research targets and highlights their potential utility as memory components in future data processing and data storage devices.[2,3] In recent years, SMM design has largely involved exploiting the magnetic anisotropy of a single metal ion with a finely tuned ligand-field environment. In contrast to the traditional "giant spin" approach in multinuclear metal complexes, designing SMMs with only a single paramagnetic ion offers the inherent advantage of simplified control of the molecular magnetic anisotropy thereby allowing the magnetic anisotropy of a single-ion to be maximized when it resides in an optimal ligand coordination environment. Although significant progress is being reported for transition metal based mononuclear SMMs,[4–6] the majority of mononuclear SMMs aim to exploit the intrinsically large single-ion magnetic anisotropy of lanthanide ions which is due to their unquenched orbital angular momentum and can lead to large magnetic moments, especially in the latter half of the lanthanide series.[7–11] Indeed, lanthanide-based SMMs can be considered the best performing SMMs to-date, especially given the family of bis-cyclopentadienyl lanthanide based cations, which led most recently to molecules that exhibit magnetic hysteresis at temperatures as high as 80 K.[12–18]

[a]*Department of Chemistry, Texas A&M University, 3255 TAMU, College Station, Texas 77843, USA. E-mail: nippe@chem.tamu.edu*

[b]*Theory of Nanomaterials Group, Katholieke Universiteit Leuven, Celestijnenlaan 200F, 3001 Leuven, Belgium. E-mail: Liviu.Chibotaru@chem.kuleuven.be*

[c]*Maastricht Science Programme, Faculty of Science and Engineering, Maastricht University, Maastricht, Netherlands*

[d]*Department of Chemistry, Wayne State University, 5101 Cass Ave, Detroit, MI 48202, USA*

† Electronic supplementary information (ESI) available: CCDC 1986607 (**1**), 1986530 (**2**), 1986548 (**2-py**), 1986581 (**2-THF***), 1986886 (**3**), 1986808 (**4**), 1986810 (**5**), 1986941 ($\mathbf{5^{iso}}$), 1986815 (**6**), 1986828 ($\mathbf{6^{iso}}$). For ESI and crystallographic data in CIF or other electronic format see DOI: 10.1039/d0sc01197e

SMM performance is highly dependent on the geometry enforced by the ligands surrounding the central ion. The ligand coordination environment dictates the height of the energy barrier to magnetization reversal ($U$) as well as influences the rate of quantum tunneling of the magnetization (QTM). For lanthanide ions, the crystal field potential acts as a perturbation on the ground spin–orbit coupled, $J$, term (within the $^{2S+1}L_J$ coupling scheme) thereby determining the energy spacing between ground and excited $m_j$ projections. In the optimal case of spin relaxation occurring by an "over-the-barrier" Orbach mechanism, the value of $U$ will be proportional to the energy gap of the ground and higher excited $m_j$ states.[19,20] Molecular symmetry also has direct bearing on the probability of QTM between resonating $m_j$ projections. In some ligand field geometries transverse anisotropy terms will be included in the crystal-field Hamiltonian, thereby resulting in rapid QTM.[21]

With this in mind, understanding how various coordination geometries affect the magnetic anisotropy a $Ln^{3+}$ ion is crucial in the continued development of high-performance SMMs. Many of the early examples of Ln-based SMMs featured multidentate oxygen and/or nitrogen-based donor ligands which naturally resulted in SMMs with high coordination numbers.[22–24] Of the "classical" Ln-SMM geometries, those featuring axially elongated square antiprismatic ($D_{4d}$),[11,25–27] axially compressed square antiprismatic ($D_{4d}$),[28,29] or compressed pentagonal bipyramidal ($D_{5h}$)[8,10,30,31] geometries have been some of the most thoroughly investigated. More recently, unique and lower coordinate structural motifs for $Ln^{3+}$ compounds have been achieved by incorporating organic based ligand scaffolds in SMM design.[32–35] Modern organometallic lanthanide chemistry has led to structurally and magnetically important molecules such as the $C_8$ symmetric lanthanide biscyclooctatetraene, $[Ln(COT)_2]^-$,[32–35] and the aforementioned pseudo and strictly linear lanthanide metallocenium, $[Ln(Cp^R)_2]^{+1/0}$, complexes.

Lanthanide-based SMMs featuring six-coordinate ligand field geometries have been relatively unexplored in terms of relating molecular geometry to the magnetic behavior of various $Ln^{3+}$ ions.[9,36–40] This is most likely due to the relatively low number of six-coordinate lanthanide complexes reported in the literature as compared to those having higher coordination numbers. Of the cubic and trigonal coordination environments for six-coordinate lanthanide compounds, a trigonal ligand field is expected to be more suitable for SMM behavior.[41] For a $Ln^{3+}$ ion residing in an idealized octahedral ($O_h$) environment, slow magnetic relaxation is not expected, as the absence of the second-order uniaxial anisotropy parameter, $B_2^0$, from the crystal-field Hamiltonian should exclude the possibility of easy-axis magnetic anisotropy.[37,42,43] In contrast, an ideal trigonal prismatic ligand field ($D_{3h}$) is predicted to stabilize a highly axial $\pm m_j$ ground state which could result in dynamic SMM behavior. Indeed, recent reports have shown that a trigonal prismatic geometry can support SMM behavior of $Dy^{3+}$ and $Tb^{3+}$ ions.[36,37,39,40,44,45]

Recently, our group utilized the organometallic chemistry of the 1,1'- diferrocenyl ($Fc^{2-}$) metallo-ligand to synthesize the first Ln-[1]ferrocenophane molecules, $[DyFc_3(THF)_2Li_2]^-$ and $[TbFc_3(THF)_2Li_2]^-$, which feature a rare trigonal prismatic arrangement of the six C1 carbons of the three dianionic $Fc^{2-}$ ligands.[44,45] $[DyFc_3(THF)_2Li_2]^-$ and $[TbFc_3(THF)_2Li_2]^-$ both exhibit zero applied field SMM behavior, with magnetic anisotropy energy barriers of $U = 110$ cm$^{-1}$ and $U = 274$ cm$^{-1}$, respectively. It is important to note that, to the best of our knowledge, $[TbFc_3(THF)_2Li_2]^-$ features the largest zero-field magnetization energy barrier for a Ln–SMM with trigonal prismatic geometry. We recognized the $[LnFc_3(THF)_2Li_2]^-$ structural motif as an ideal template for investigating the relationship between trigonal prismatic molecular geometry and the magnetic anisotropy of the rest of the late $Ln^{3+}$ ions. The homoleptic coordination environment of $[LnFc_3(THF)_2Li_2]^-$ leads to higher symmetry compared to many of the previously reported trigonal prismatic SMMs which contain hetero-ligand donor atoms.

Herein, we report the synthesis, structural, and magnetic characterization of the late Ln-[1]ferrocenophane complexes, $[Li(THF)_4][LnFc_3(THF)_2Li_2]$ (Ln = Gd (**1**), Ho (**2**), Er (**3**), Tm (**4**), Yb (**5**), Lu (**6**)). Of the compounds reported, the Ho-[1]ferrocenophane compound $[HoFc_3(THF)_2Li_2]^-$ exhibits slow magnetic relaxation in the absence of externally applied dc fields which renders it a rare example of a non-Kramers $Ho^{3+}$ SMM. Furthermore, we show how small distortions in the trigonal prismatic ligand field can lead to dramatic differences in magnetization dynamics of the Ho-[1]ferrocenophane structural motif by synthesizing and magnetically characterizing the pyridine (py) and 2-methyl THF (THF*) solvent adducts, $[Li(py)_4][HoFc_3(py)_2Li_2]$ (**2-py**) and $[Li(THF^*)_4][HoFc_3(THF^*)_2Li_2]$ (**2-THF***), respectively. Compounds **1–6** were also investigated by *ab initio* computational methods which provided further insight into the electronic structure of the $Ln^{3+}$ ions residing in a trigonal prismatic ligand field geometry and their observed static and dynamic magnetic properties.

## Results and discussion

### Synthesis

The late Ln-[1]ferrocenophane compounds $[Li(THF)_4][LnFc_3Li(THF)_2]$ (Ln = Gd (**1**), Ho (**2**), Er (**3**), Tm (**4**), Yb (**5**), or Lu (**6**)) were prepared using a previously reported protocol *via* the salt elimination reaction of anhydrous $LnCl_3$ with excess $Li_6Fc_3(TMEDA)_2$ (TMEDA = tetramethylethylenediamine) in THF (Fig. 1).[44,45] Crude **1–6** are moderately soluble in $Et_2O$ which allows for their facile separation from insoluble unreacted starting materials and/or biproducts. Following an $Et_2O$ extraction, crude **1–6** are recrystallized by slow diffusion of pentane into their concentrated THF solutions, forming highly air and moisture sensitive plate crystals of **1–6** in yields between 21–91% (based on Ln). The relatively high yield of the Tm-[1]ferrocenophane compound **4** (91%), is an outlier and could be a result of the $Tm^{3+}$ six-coordinate ionic radii (0.880 Å) being the optimal size for the $[LnFc_3]^{3-}$ coordination environment. Compound **1** can also be synthesized using anhydrous $GdI_3$ but in lower yields due to difficult separation of $(THF)_xLiI$ or $[(TMEDA)_2LiI]_2$ salt biproducts. Furthermore, depending on the crystallinity of the $LnCl_3$ salt, higher yields are obtained for

compounds **1–6** by forming the $LnCl_3(THF)_x$ solvate prior to addition to $Li_6Fc_3(TMEDA)_2$.

The low temperature crystallization of the heaviest Yb- and Lu-[1]ferrocenophane complexes **5** and **6** resulted in a mixture of crystals with two habits: crystals of plate and rod-like shapes could easily be identified. Analysis of both morphologies *via* single-crystal X-ray diffraction (*vide infra*) determined the rod-shaped crystals to contain structurally unique solvate of the $[LnFc_3(THF)_2Li_2]^-$ anion (hereon denoted as $\mathbf{5^{Iso}}$ and $\mathbf{6^{Iso}}$) whereas the plate crystals are isostructural to **1–4**. The crystalline structure of $\mathbf{5^{Iso}}$ and $\mathbf{6^{Iso}}$ differs from **5** and **6** by means of an extra THF solvate molecule located in the crystal lattice. The formation of multiple solvates is unique to the preparation of **5** and **6** and could be a consequence of the ionic radii of $Yb^{3+}$ and $Lu^{3+}$ being the smallest of the 4f series.

The diamagnetic nature of the $4f^{14}$ electron configuration of the $Lu^{3+}$ ion allows for facile analysis of the solution phase structure of **6** and $\mathbf{6^{Iso}}$ by $^1$H-NMR spectroscopy. The $^1$H-NMR spectrum of a mixture of **6** and $\mathbf{6^{Iso}}$ in THF-$d_8$ shows nearly identical chemical shifts as the previously reported $[Li(THF)_4][YFc_3(THF)_2Li_2]$ compound, with two downfield resonances at 4.05 ppm and 4.09 ppm corresponding to the two sets magnetically inequivalent protons of the diferrocenyl ligands (Fig. 1). The presence of only two resonances corresponding to the $Fc^{2-}$ ligand protons suggest the solution phase structures of **6** and $\mathbf{6^{Iso}}$ are similar on the NMR measurement timescale.

Once crystalized, compounds **1–6** are highly insoluble in nonpolar alkanes and ethers such as pentane, diethyl ether, and 1,4-dioxane as well as weakly or non-coordinating polar solvents, such as difluorobenzene. In contrast, **1–6** are highly soluble in polar coordinating solvents such as THF, 2-methyl THF (THF*) and pyridine (py). The solubility properties of **1–6** suggest that dissolution could involve coordination of the polar coordinating solvent to the $Li^+$ ions within the lattice of **1–6**. Therefore, we hypothesized that various solvent adducts of the

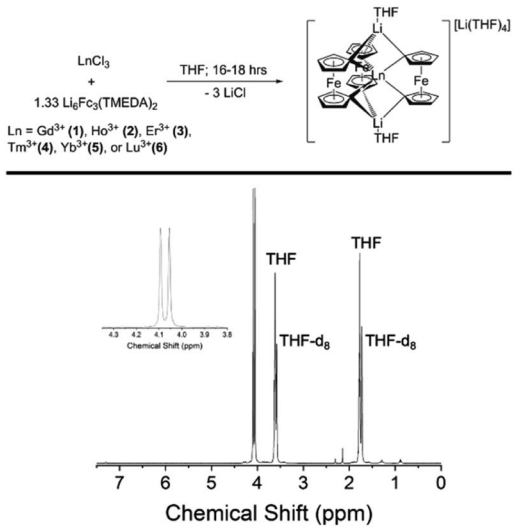


Fig. 1 (Top) Preparation of late Ln-[1]ferrocenophane compounds. (Bottom) $^1$H NMR (400 MHz, THF-$d_8$) of the Lu-[1]ferrocenophane compound **6**.

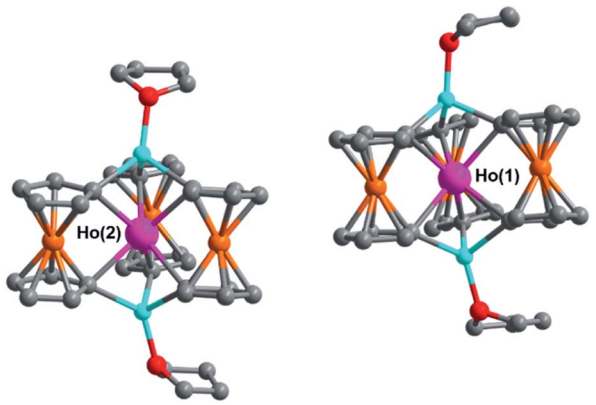


Fig. 2 Molecular structure of the two crystallographically unique $[HoFc_3(THF)_2Li_2]^-$ complexes of **2**. Hydrogen atoms and $[Li(THF)_4]^+$ counter cations removed for clarity. Pink = Ho, orange = Fe, blue = Li, red = O, grey = C.

general formula $[Li(sol)_x][LnFc_3(sol)_2Li_2]$, where sol is a polar coordinating solvent, could be synthesized. Indeed, the synthesis of the Ho-[1]ferrocenophane solvent adducts, $[Li(py)_4][HoFc_3(py)_2Li_2]$ (**2-py**) and $[Li(THF^*)_4][HoFc_3(THF^*)_2Li_2]$ (**2-THF***), was achieved by slow diffusion of pentanes into pyridine and 2-methyl THF solutions of $[Li(THF)_4][HoFc_3(THF)_2Li_2]$, respectively. Single crystal X-ray diffraction studies of **2-py** and **2-THF*** (*vide infra*) reveal that for **2-py** all coordinated THF molecules have been replaced by pyridine molecules. On the other hand, the structure of **2-THF*** indicates significant disorder in the THF* solvate molecules which could suggest a statistical mixture of $[Li–THF]^+$ and $[Li–THF^*]^+$ units within the same crystal lattice.

## Solid state structural determination

**Solid state structures of 1–6, $\mathbf{5^{Iso}}$, and $\mathbf{6^{Iso}}$.** The solid-state structures of compounds **1–6** were determined *via* single-crystal X-ray diffraction and are isostructural to the previously reported $Tb^{3+}$ and $Dy^{3+}$ congeners. All six compounds crystalize in the monoclinic space group $P2_1/c$ inside a highly anisotropic unit cell ($a$,$c$ < 15 Å and $b$ > 60 Å). The molecular structure of **1–6** features a single $Ln^{3+}$ ion accommodated by three dianionic ferrocenyl ligands ($Fc^{2-}$) that are arranged in a distorted $C_3$ fashion around the central $Ln^{3+}$ ion (Fig. 2). The six-coordinate geometry of each Ln-[1]ferrocenophane molecule is most accurately described as distorted trigonal prismatic with the principal $C_3$ axis passing through the centroids of the three diferrocenyl C1-carbons, forming a tri-anionic "pocket" above and below the equatorial plane of the molecule. Each charged ligand "pocket" is stabilized by a $[Li–THF]^+$ moiety which completes the inner-sphere, $[LnFc_3(THF)_2Li_2]^-$, monoanionic complex. The molecular charge is balanced by a $[Li(THF)_4]^+$ unit residing in the outer-sphere.

The unit cells of **1–6** contain two structurally unique Ln-[1]ferrocenophane molecules per asymmetric unit (**Ln(1)** and **Ln(2)**), each having similar bonding parameters (Table 1). Across the series the average Ln–C bond distances decrease

 

Table 1 Selected average interatomic distances and angles for compounds **1–6**

| Compound | **1 (Gd)** | **2 (Ho)** | **3 (Er)** | **4 (Tm)** | **5 (Yb)** | **6 (Lu)** |
|---|---|---|---|---|---|---|
| **Ln(1)**–C, Å | 2.572[8] | 2.532[13] | 2.521[9] | 2.520[5] | 2.499[17] | 2.501[11] |
| **Ln(2)**–C, Å | 2.569[8] | 2.539[12] | 2.522[9] | 2.517[5] | 2.503[16] | 2.497[11] |
| **Ln(1)**···Fe, Å | 3.2281[12] | 3.229[8] | 3.2196[14] | 3.214[8] | 3.213[2] | 3.2108[16] |
| **Ln(2)**···Fe, Å | 3.2300[12] | 3.221[13] | 3.2172[14] | 3.212[8] | 3.209[2] | 3.2068[16] |
| **Ln(1)** C1–Fe–C1, ° | 105.3[3] | 103.5[5] | 102.9[4] | 103.1[2] | 102.1[7] | 102.2[4] |
| **Ln(2)** C1–Fe–C1, ° | 104.9[3] | 103.8[5] | 103.1[4] | 103.0[2] | 102.3[7] | 102.1[1] |
| C–**Ln(1)**–C, ° | 80.9[3] | 81.3[4] | 80.7[3] | 80.9[2] | 81.0[6] | 80.8[4] |
| C–**Ln(2)**–C, ° | 81.0[3] | 81.3[4] | 80.8[3] | 81.0[2] | 81.1[6] | 81.1[4] |
| **Ln(1)**, $Fc^{2-}$ twist, ° | 8.16 | 10.67 | 11.57 | 12.76 | 13.18 | 14.24 |
| **Ln(2)**, $Fc^{2-}$ twist, ° | 9.64 | 12.67 | 14.49 | 16.23 | 16.65 | 18.56 |

from 2.572[8] Å and 2.569[8] Å for 1 (**Gd(1)** and **Gd(2)**, respectively) to 2.501[11] Å and 2.497[11] Å for compound **6** (**Lu(1)** and **Lu(2)**, respectively). The observed decrease in Ln–C bond distance with increase in atomic number is most likely due to the increased Lewis acidity and/or the smaller ionic radii of the heaviest $Ln^{3+}$ ions. The intramolecular Ln···Fe distances show a more subtle change across the period decreasing from 3.2281[12] Å and 3.2300[12] Å for **1** (**Gd(1)** and **Gd(2)**, respectively) to 3.2108[16] Å and 3.2068[16] Å for **6** (**Lu(1)** and **Lu(2)**, respectively). The average Ln···Fe distances between 3.2300[12] to 3.2068[16] Å are some of the closest reported for any heterometallic Ln–Fe species, but lie just outside the sum of the covalent radii of the $Fe^{2+}$ and $Ln^{3+}$ ions.[46]

Despite miniscule differences in the average bonding parameters between the distinct **Ln(1)** and **Ln(2)** molecules within each unit cell of **1–6**, each molecule shows significant differences of the average $Fc^{2-}$ ligand twist angle. Here, the ligand twist angle is defined by the torsion of the two C1 donor atoms of a single diferrocenyl ligand with respect to the centroids (previously described) of the trianionic pockets located above and below equatorial plane of the molecule (see Fig. 3 left inset). A ligand twist angle greater than 0° would indicate distortion of the molecular geometry away from ideal trigonal prismatic geometry. For the **Ho(1)** and **Ho(2)** molecules of compound **2**, the average ligand twist angles are 10.67° and 12.67°, respectively. It is important to note here that such small differences in the ligand field geometry can greatly influence the spectroscopic and magnetic characteristics of a $Ln^{3+}$ ion.[47,48] Considering the **Ln(2)** molecules across the heavy lanthanide series, the average diferrocenyl twist angle has an inversely proportional relationship to the 6-coordinate ionic radius of the $Ln^{3+}$ ion, increasing from 9.64° for **Gd(2)** ($r_{Gd^{3+}}$ = 0.938 Å) to

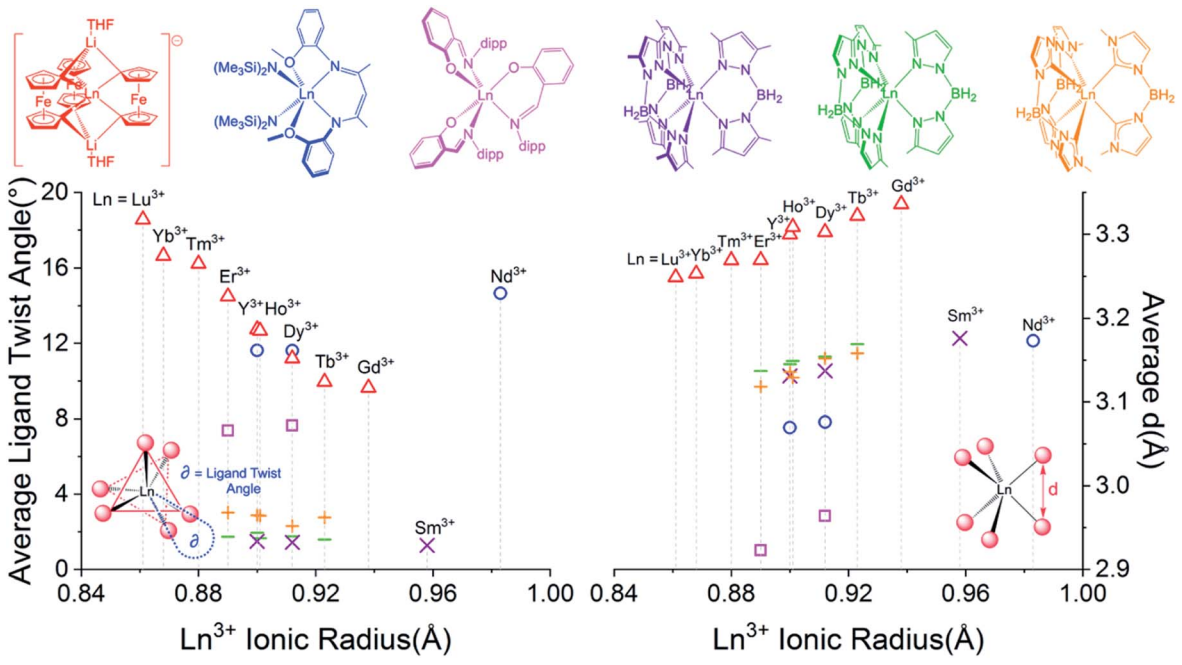


Fig. 3 (Left) Ligand twist angle dependence on $Ln^{3+}$ ionic radius of **Ln(2)** molecules of $[LnFc_3(THF)_2Li_2]^-$ and selected previously reported trigonal prismatic lanthanide complexes. (Right) Dependence of average ligand donor distance, d (defined in right inset), on the $Ln^{3+}$ ionic radius. Triangles = **Ln(2)** of **1–6** ($[YFc_3(THF)_2Li_2]^-$ included from ref. 51), squares = $[Ln(L)_3]$, circles = $[(L^{CO})Ln(N(SiMe_3)_2)_2]$, crosses = $Ln(Bc^{Me})_3$, lines = $Ln(Bp^{Me})_3$, and X = $Ln(Bp^{2Me})_3$ ($Y^{3+}$ compounds included for selected examples).

18.56° for **Lu(2)** ($r_{Lu^{3+}} = 0.861$ Å). The **Ln(1)** molecules across the period show an identical trend. This inverse relationship between twist angle and ionic radius can be explained by the increased steric hindrance of the $[Fc_3]^{6-}$ ligand field as the $Ln^{3+}$ ionic radius decreases and the needed 'twist' of the $Fc^{2-}$ ligands to stabilize the smaller $Ln^{3+}$ center.

For the trigonal prismatic geometry, comparison of the distance, *d*, between eclipsed ligand donor atoms or pseudo eclipsed donors (in the case of a ligand twist angle > 0) for a series of similar complexes can indicate the degree of ligand rigidity as well as the axiality trigonal ligand field of the central $Ln^{3+}$ ion. In the case of $[LnFc_3(THF)_2Li_2]^-$, *d* would be the distance between the two C1 donors of a single $Fc^{2-}$ ligand (see Fig. 3 right inset) and is proportional to the C–Ln–C bite angle. For the **Ln(2)** molecules of **1–6**, the largest average *d* value of the three $Fc^{2-}$ ligands is 3.336 Å for **1** which features the largest $Gd^{3+}$ ion. Upon moving across the row, the average C1···C1 distance of the $Fc^{2-}$ ligand decreases to a value of 3.249 Å for **6** (Fig. 3 right). The decrease in average $Fc^{2-}$ C1···C1 distance with decrease in $Ln^{3+}$ ionic radii is accompanied by a decrease in the average C1–Fe–C1 angle of the $Fc^{2-}$ ligand from 104.9°[3] for the **Gd(2)** in **1** to 102.1°[1] for **Lu(2)** in **6**.

In order to gain a more comprehensive picture of the geometric trends in trigonal prismatic lanthanide compounds, we compared the average ligand twist angle and *d* values of **1–6** with the same parameters of selected previously reported trigonal prismatic lanthanide complexes $[(L^{CO})Ln(N(SiMe_3)_2)_2]$ ($HL^{CO}$ = {*N*-[(2-MeO)-$C_6H_5$]}N=C(Me)CH=C(Me)N(H){N'-[(2-MeO)$C_6H_5$]}; Ln = $Nd^{3+}$, $Dy^{3+}$, or $Y^{3+}$),[37,49] $[Ln(L)_3]$ (HL = 2-(((2,6-diisopropylphenyl)imino)methyl)-phenol; Ln = $Dy^{3+}$ or $Er^{3+}$),[36] $Ln(Bp^{Me_2})_3$ ($[Bp^{Me_2}]^-$ = dihydrobis(dimethylpyrazole)borate; Ln = $Sm^{3+}$, $Dy^{3+}$, or $Y^{3+}$),[39,50] $Ln(Bp^{Me})_3$ ($[Bp^{Me}]^-$ = dihydrobis(methylpyrazole)borate; Ln = $Tb^{3+}$, $Dy^{3+}$, $Y^{3+}$, $Ho^{3+}$, or $Er^{3+}$), and $Ln(Bc^{Me})_3$ ($[Bc^{Me}]^-$ = dihydrobis(methylimidazolyl) borate; Ln = $Tb^{3+}$, $Dy^{3+}$, $Y^{3+}$, $Ho^{3+}$, or $Er^{3+}$)[40] (Fig. 3). Of the compared complexes, **1–6**, $Ln(Bp^{Me_2})_3$, $Ln(Bp^{Me})$, and $Ln(Bc^{Me})_3$ feature a homo-ligand donor environment around the central $Ln^{3+}$ ions. To this end, for the tris-pyrazolyl and tris-imidazolyl borate complexes, the possibility of HB–H···Ln agostic interactions complicate a complete structural comparison with these compounds. Upon inspection of Fig. 3 (Left), it is apparent that the Ln-[1]ferrocenophane complexes, **1–6**, feature the greatest susceptibility of ligand twist angle with a change in ionic radius. Furthermore, in contrast to the Ln-[1]ferrocenophane series, $[(L^{CO})Ln(N(SiMe_3)_2)_2]$, $[Ln(L)_3]$, $Ln(Bp^{Me_2})_3$, $Ln(Bp^{Me})_3$, and $Ln(Bc^{Me})_3$ feature an increase of the average ligand twist angle with $Ln^{3+}$ ionic radius or do not show a significant correlation at all (in the case of the tris–borate complexes).

In general, all five sets of compared trigonal prismatic lanthanide complexes exhibit an increase in the average eclipsed/pseudo eclipsed ligand donor distanced, with an increase in $Ln^{3+}$ ionic radii (Fig. 3, right). Despite this similar trend, the Ln-[1]ferrocenophane complexes, **1–6**, feature the largest average *d* values of the compared complexes. This distinction is significant and could suggest the $Fc^{2-}$ donor ligands of **1–6** might interact more strongly with f-orbitals of *z*-character, which in turn would have a significant influence of the magnetism of these compounds.

The single-crystal X-ray structures for the $Yb^{3+}$ and $Lu^{3+}$ solvates, $\mathbf{5^{Iso}}$ and $\mathbf{6^{Iso}}$, were solved in the monoclinic space group $I_a$ and *Cc*, respectively, inside a unit cell with lengths between 20–33 Å. Though solved in different space groups, $\mathbf{5^{Iso}}$ and $\mathbf{6^{Iso}}$ are most likely isostructural given the almost identical unit cell volumes of 16 344(3) $Å^3$ (for $\mathbf{5^{Iso}}$) and 16 419(4) $Å^3$ (for $\mathbf{6^{Iso}}$) (see ESI† for details). Both $\mathbf{5^{Iso}}$ and $\mathbf{6^{Iso}}$ contain three structurally unique $[Li(THF)_4][LnFc_3(THF)_2Li_2]$ molecules per unit cell along with an uncoordinated THF lattice solvate per Ln-[1]ferrocenophane molecule which is not present in compounds **5** and **6** (Fig. 4). The average Ln–C and Ln···Fe distances for the three independent molecules of $\mathbf{5^{Iso}}$ and $\mathbf{6^{Iso}}$ are close to the corresponding distances for the two independent molecules of compound **5** and **6**, respectively (Table S12†). To this end, the average $Fc^{2-}$ twist angles vary significantly between corresponding solvates. The most distorted molecules of the THF solvated molecules, $\mathbf{5^{Iso}}$ and $\mathbf{6^{Iso}}$, exhibit a 3.3° and a 2.4° increase in twist angle when compared to the most highly distorted molecules of **5** and **6**, respectively. This result is significant as it highlights how crystal packing effects can greatly influence the geometry of the inner coordination sphere of the individual molecules in the solid state.

**Solid state structures of 2-THF* and 2-py.** The single crystal X-ray structures of the Ho-[1]ferrocenophane THF* and pyridine adducts, **2-THF*** and **2-py**, were solved in the monoclinic and orthorhombic space group $P2_1/n$ and $P2_12_12_1$, respectively. Both **2-THF*** and **2-py** feature a $[HoFc_3(sol)_2Li_2]^-$ core similar to that

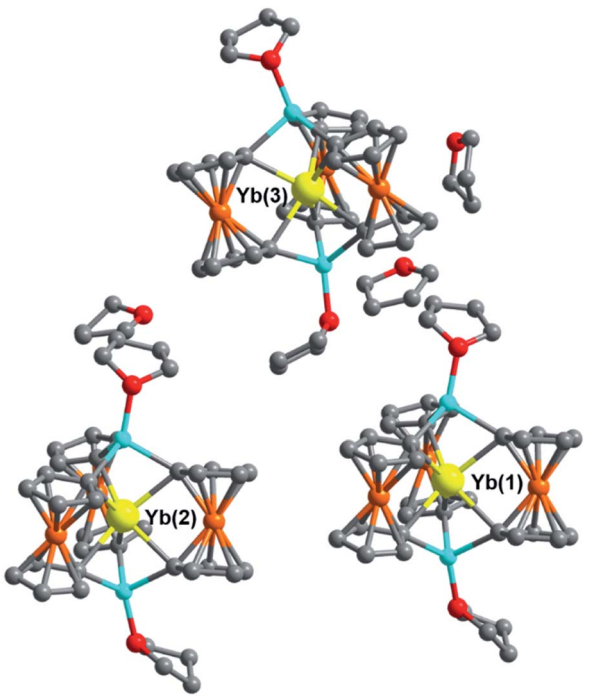


Fig. 4 Molecular structure of the three crystallographically unique $[YbFc_3(THF)_2Li_2]^-$ complexes of $\mathbf{5^{Iso}}$ and THF solvate molecules. Hydrogen atoms and $[Li(THF)_4]^+$ counter cations removed for clarity. Yellow = Yb, orange = Fe, blue = Li, red = O, grey = C.

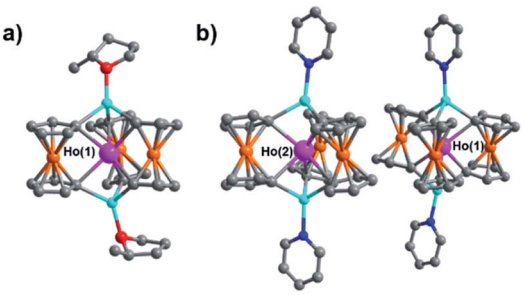


Fig. 5 Molecular structure of 2-THF* (a) and the two crystallographically unique $[HoFc_3(py)_2Li_2]^-$ complexes of 2-py (b). Hydrogen atoms and $[Li(sol)_4]^+$ counter cations removed for clarity. Pink = Ho, orange = Fe, blue = Li, red = O, dark blue = N, grey = C.

of compound 2 except with displaced THF molecules of the [Li–THF]$^+$ units with THF* (for **2-THF***) or pyridine (for **2-py**) (Fig. 5). Substitution of inner sphere THF molecules with THF* or pyridine do not significantly change the Ho–C bond distances which are within error equal to those of compound 2 (Table S13†). To this end, the Ho···Fe distances decrease from 3.229[8] and 3.221[13] for **Ho(1)** and **Ho(2)** in 2 to 3.2098[13] Å for **2-THF*** to 3.1970[15] Å and 3.1617[16] Å for **Ho(1)-py** and **Ho(2)-py** in **2-py**. In contrast to compound 2, the unit cell of **2-THF*** contains only a single structurally unique $Ho^{3+}$ site. Significant disorder of the THF* molecules was observed in the X-ray structure **2-THF*** which is likely a result of multiple orientations of the coordinated THF* molecule. It should also be noted that the observed disorder could also suggest incomplete displacement of the THF molecules upon dissolution of compound 2 in THF*. To this end, the atoms of the $[HoFc_3Li_2]^-$ core do not show signs of disorder which might have been expected considering the differing donor strengths of the THF and THF*. Similar to 2, the unit cell of **2-py** features two structurally unique $Ho^{3+}$ sites. Only positional disorder of the inner sphere pyridine solvate molecules of the [Li–py]$^+$ unit is observed in the X-ray structure which suggest full displacement of the THF molecules upon dissolution of 2 in pyridine.

Though little variation is observed in the interatomic Ho–C distances between 2, **2-THF***, and **2-py**, the average $Fc^{2-}$ twist angle varies significantly upon changing the identity of the axial [Li-sol]$^+$ moiety. Considering the most highly distorted molecule within each of the unit cells, the average $Fc^{2-}$ twist angle increases from 12.67° (for 2), to 16.52° (for **2-THF***), to 23.69° (for **2-py**) (Fig. 6). The average $Fc^{2-}$ twist angle for **2-py** represents the largest of any of the Ln-[1]ferrocenophane compounds reported herein. As shown previously with the structural variation between the corresponding solvates of the Yb- and Lu-[1]ferrocenophane complexes, crystal packing can greatly influence the geometry of the $[LnFc_3(THF)_2Li_2]^-$ inner coordination sphere. The variation in the crystal packing for 2, **2-THF***, and **2-py** is also emphasized by the changes in the closest intermolecular distances between $Ho^{3+}$ sites of 10.586 Å (for 2), 11.069 Å (for **2-THF***), and 8.941 Å (for **2-py**) (Table S14†). The varying electronic donor strengths of the solvent molecules likely plays an additional role in the geometric variation between 2, **2-THF***, and **2-py** though similar Li–C and Li···Ho interatomic distance between the molecules precludes any further discussion here.

## Magnetic properties

**Static magnetic properties of $[Li(THF)_4][LnFc_3(THF)_2Li_2]$ (1–5/5$^{Iso}$).** The static magnetic properties of compounds **1–5** were investigated by measuring the temperature dependence of the molar magnetic susceptibility under an external 0.1 T magnetic field across the 300–2 K temperature range (Fig. 7). The $\chi_M T$ (300 K) values for **2–5** are 14.39 emu K mol$^{-1}$ (2), 11.71 emu K mol$^{-1}$ (3), 7.00 emu K mol$^{-1}$ (4), and 2.50 emu K mol$^{-1}$ (5) and correspond nicely to the expected values of 14.07 emu K mol$^{-1}$,

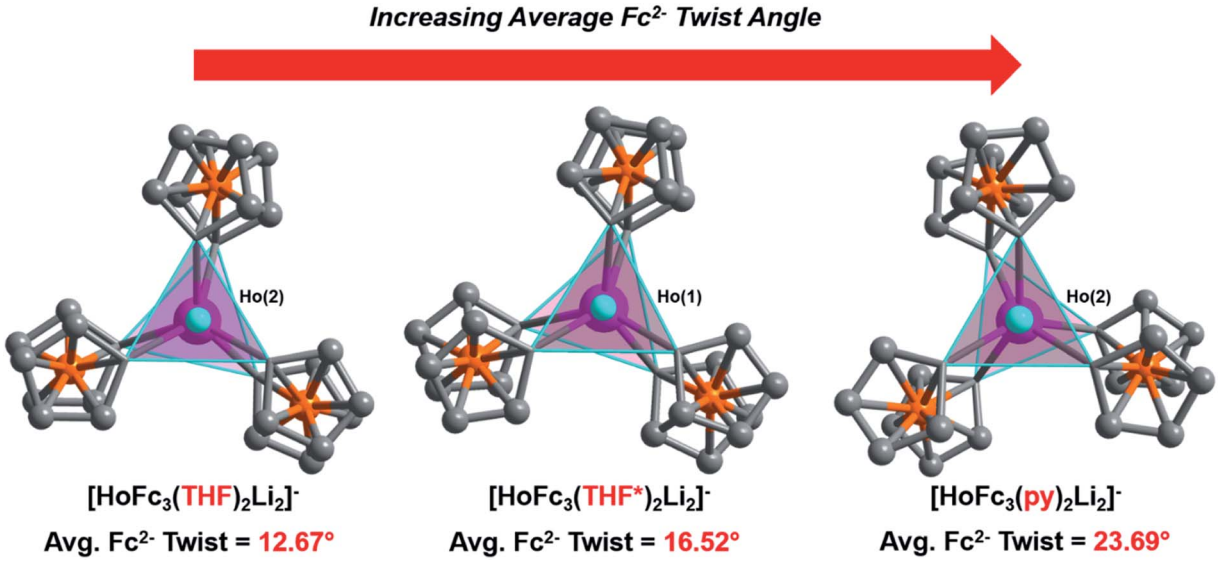


Fig. 6 Comparison of the average twist angle of the $Fc^{2-}$ ligands in 2, **2-THF***, and **2-py** viewed down the Li–Ho–Li axis. Coordinated THF, THF*, and pyridine molecules removed for clarity.

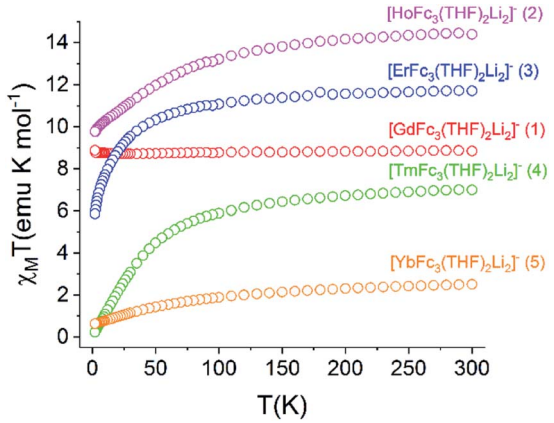


Fig. 7 Temperature dependence of the $\chi_M T$ of **1–5/5$^{Iso}$** ($H = 0.1$ T, $T =$ 2–300 K).

11.48 emu K mol$^{-1}$, 7.15 emu K mol$^{-1}$, and 2.57 emu K mol$^{-1}$ for a single non-interacting $Ho^{3+}$ ($^5I_8$; $S = 2$, $L = 6$; $g_J = 5/4$), $Er^{3+}$ ($^4I_{15/2}$; $S = 3/2$, $L = 6$; $g_J = 6/5$), $Tm^{3+}$ ($^3H_6$; $S = 1$, $L = 5$; $g_J = 7/6$), and $Yb^{3+}$ ($^2F_{7/2}$; $S = 1/2$, $L = 3$; $g_J = 8/7$) ions, respectively. The $\chi_M T$ (300 K) value of 1 is 8.84 emu K mol$^{-1}$ and is slightly higher than the expected value of 7.88 emu K mol$^{-1}$ for a non-interacting $Gd^{3+}$ ion ($^8S_{7/2}$; $S = 7/2$, $L = 0$; $g_J = 2$). This discrepancy could be due to small weighing errors or a preferred orientation of the Gd-[1]ferrocenophane plate crystallites aligning with the external field, resulting in a slight increase of the magnetic moment. Upon cooling, the $\chi_M T$ of **1** remains constant across the entire temperature range suggesting an isolated $S = 7/2$ ground state and weak intermolecular magnetic interactions between neighboring molecules in the crystal lattice. In contrast, deviation from typical Curie–Weiss behavior is observed for **2–5**. For the $Ho^{3+}$ and $Yb^{3+}$ compounds **2** and **5**/**5$^{Iso}$**, the $\chi_M T$ value remains nearly constant until *ca.* 100 K where a gradual decrease is observed to minimum values of 9.77 emu K mol$^{-1}$ (for **2**) and 0.63 emu K mol$^{-1}$ (for **5**) at 2.5 K and 2 K, respectively. A steeper $\chi_M T$ decline at low temperatures is observed for **3**, where a drop from 11.08 emu K mol$^{-1}$ to 5.86 emu K mol$^{-1}$ occurs between 100–2 K. The most pronounced temperature dependent behavior is observed for the $Tm^{3+}$ compound **4** which exhibits a nearly linear decrease of $\chi_M T$ with temperature beginning at 30 K to a minimum value of 0.23 emu K mol$^{-1}$ at 2 K. The low temperature decline of the $\chi_M T$ value observed for **2–5** is typical for mono-metallic species containing a single anisotropic $Ln^{3+}$ ion and is commonly attributed to the depopulation of the crystal field states, very weak intermolecular antiferromagnetic interactions, and/or blocking of the magnetization. However, the precipitous drop of the $\chi_M T$ value of **4** suggest population of a non-magnetic ground state at the lowest temperatures. This observation is further supported by *ab initio* calculations which predicts a stabilization of a $m_j = 0$ ground state of the $Tm^{3+}$ ion within the crystal field sublevels (*vide infra*).

The static magnetic behavior of **1–5** was further investigated by measuring the field dependence of the magnetization between 2–8 K (Fig. S12†). For compounds **2–5**, the 2 K magnetization values at the 7 T field limit are 5.11 $\mu_B$ (for **2**), 6.16 $\mu_B$ (for **3**), 1.28 $\mu_B$ (for **4**), and 1.36 $\mu_B$ (for **5**), respectively, and are much lower than the expected single ion $M_s$ values of 10 $\mu_B$ (for $Ho^{3+}$), 9 $\mu_B$ (for $Er^{3+}$), 7 $\mu_B$ (for $Tm^{3+}$), and 4 $\mu_B$ (for $Yb^{3+}$). This discrepancy suggests anisotropy of the lowest energy J

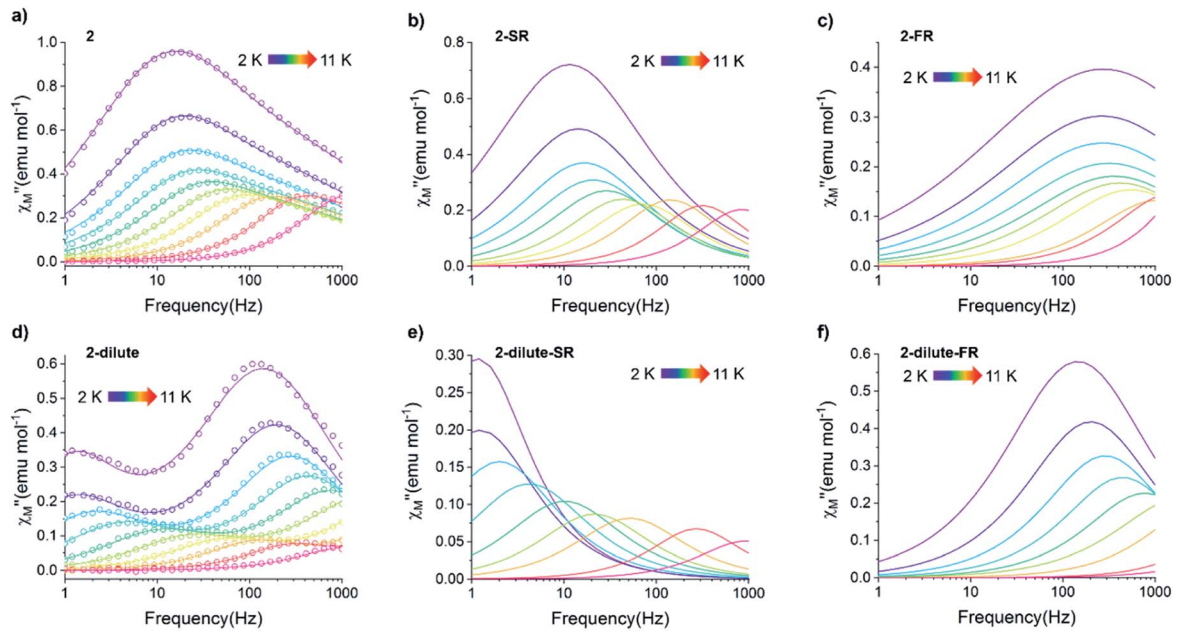


Fig. 8 (a–c) Temperature dependence of the out-of-phase component of the molar ac magnetic susceptibility ($\chi_M''$) of **2** (a) and the corresponding resolved slow (b) and fast (c) relaxation processes. (d–f) Temperature dependence of the out-of-phase component of the molar ac susceptibility ($\chi_M''$) of **2-dilute** and the corresponding resolved slow (e) and fast (f) relaxation processes ($H = 0$ T, $T = 2$–11 K). Lines represent fits to the experimental data (circles) or resolved **SR** and **FR** data.

 

multiplets of the respective $Ln^{3+}$ ion which results in non-degenerate $m_j$ microstates. The inherent magnetic anisotropy of **2–5** is further supported by the non-superposition of the *M vs. H*/*T* curves between 2–8 K (Fig. S13†). For compound **1**, the 2 K magnetization curve reaches a maximum value of 7.78 $\mu_B$ at 7 *T* which corresponds nicely to the expected value of 7 $\mu_B$ for a single $Gd^{3+}$ ion. This data along with the superposition of the *M vs. H*/*T* curves between 2–8 K supports the isotropic nature of an isolated $S = 7/2$ ground state in **1**.

**Dynamic magnetic properties of $[Li(THF)_4][HoFc_3(THF)_2Li_2]$ (2).** Examples of mononuclear Ho-based molecules that display dynamic magnetic behavior are relatively sparse in the literature.[28,52–57] Even rarer are holmium SMMs which are supported by purely organic based ligand field environments.[58,59] The rarity of Ho-based SMMs is likely due to $Ho^{3+}$ being a non-Kramers ion, which does not necessitate a degenerate magnetic ground state as in $Dy^{3+}$, $Er^{3+}$, or $Yb^{3+}$ based molecules. Furthermore, the 100% natural abundance of the $I = 7/2$ $^{165}$Ho nuclei facilitates strong nuclear hyperfine interactions which can cause fast QTM.[60]

A common characteristic among the few reported Ho-based SMMs is a highly symmetric axial ligand field environment which stabilizes a suitably anisotropic $m_j$ ground state of the oblate $Ho^{3+}$ ion. Previous *ab initio* studies of the Dy- and Tb-[1]ferrocenophane compounds suggest the three diferrocenyl ligands of $[LnFc_3(THF)_2Li_2]^-$ promote a largely axial ligand field that stabilizes large $m_j$ ground states in the oblate $Dy^{3+}$ and $Tb^{3+}$ ions. Based on these results, we hypothesized that the trigonal prismatic $[Fc_3]^{6-}$ ligand field could be suitable to promote a highly anisotropic ground state in the oblate $Ho^{3+}$ ion resulting in SMM behavior in the $[HoFc_3(THF)_2Li_2]^-$ complex. In order to probe the SMM behavior in **2**, the variable temperature alternating current (ac) magnetic susceptibility was measured in the absence of an external magnetic field. The presence of a broad temperature dependent signal in the molar out-of-phase component ($\chi''_M$) of the ac magnetic susceptibility *versus* frequency plot indicates **2** is indeed a rare example of zero applied field $Ho^{3+}$ SMM (Fig. 8a). Between 2–5 K, the $\chi''_M$ signal maximum is slightly temperature dependent, shifting to higher frequencies upon increasing the temperature. This slight variation of the $\chi''_M$ maximum with temperature is significant as it suggests contributions to the spin relaxation from thermally assisted Raman and/or Orbach mechanisms even at the lowest temperatures. Increasing the temperature above 5 K, the $\chi''_M$ maximum becomes increasingly temperature dependent, moving outside the 1000 Hz frequency limit at 11 K.

The exceptionally broad nature of the $\chi''_M$ signal of **2** indicates multiple spin relaxation processes are occurring at similar ac frequencies.[61] It is likely that this observation is predominately a result of the two structurally unique **Ho(1)** and **Ho(2)** sites in the solid state structure of **2** having slightly different magnetization dynamics. However, the complexity of the spin dynamics of Ln–SMMs has recently been emphasized and the simultaneous contribution from Raman, Orbach, and QTM processes to the spin relaxation of a single $Ho^{3+}$ ion cannot be excluded.[62] The molar in-phase ($\chi'_M$) and the out-of-phase ($\chi''_M$) components of the ac magnetic susceptibility of **2** were used to construct Cole–Cole plots ($\chi''_M$ *vs.* $\chi'_M$) at each temperature which were subsequently fit with eqn (1):

$$\chi_{AC}(\omega) = \chi_{S,tot} + \frac{\Delta\chi_1}{1 + (i\omega\tau_1)^{(1-\alpha_1)}} + \frac{\Delta\chi_2}{1 + (i\omega\tau_2)^{(1-\alpha_2)}} \quad (1)$$

(Cole–Cole parameters defined in ESI†). Eqn (1) represents the sum of two modified Debye functions and describes two magnetic relaxation processes each having a characteristic magnetic relaxation time, $\tau_1$ and $\tau_2$, at each temperature.

Using the extracted Cole–Cole parameters at each temperature, a "slow" (**SR**) and a "fast" (**FR**) relaxation process could be resolved in the $\chi''_M$ *versus* frequency plot of **2**, where the 2 K $\chi''_M$ signal maxima of **SR** and **FR** appear at 11.6 and 262.5 Hz, respectively (Fig. 8b and c). For **FR**, the shorter 2 K magnetic relaxation time of $\tau_2 = 0.00058$ s (as compared to $\tau_1 = 0.014$ s for **SR**) and the temperature independence of the $\chi''_M$ signal maximum suggests significant contribution of QTM to the spin relaxation. The origin of the increased QTM contribution for **FR** is most likely due to transverse fields arising from intermolecular interactions between neighboring spin centers or nuclear hyperfine interactions.

To further investigate the origin of QTM in **2**, the magnetically dilute species, $[Li(THF)_4][Y_{0.94}Ho_{0.06}Fc_3(THF)_2Li_2]$ (**2-dilute**), was prepared and magnetically characterized. Similar to **2**, the zero-field ac magnetic susceptibility data of **2-dilute** provides evidence of multiple spin relaxation processes, with two distinct maxima appearing at 1.2 Hz and 107.8 Hz in the $\chi''_M$ *vs.* Frequency plot at 2 K (Fig. 8d). As previously described, a **FR** and **SR** process were resolved by fitting the ac magnetic susceptibility of **2-dilute** with eqn (1) (Fig. 8e amd f). The 2 K magnetic relaxation times of $\tau_1 = 0.14$ s (for **SR**) and $\tau_2 = 0.0011$ s (for **FR**) are at least half of an order of magnitude longer than the corresponding **SR** and **FR** processes for non-dilute **2** at the same temperature. This result is significant as it suggests that intermolecular magnetic interactions are playing a non-negligible role in the low temperature magnetization dynamics of compound **2**. To this end, the $\chi''_M$ maximum of the **SR** processes of **2-dilute** at

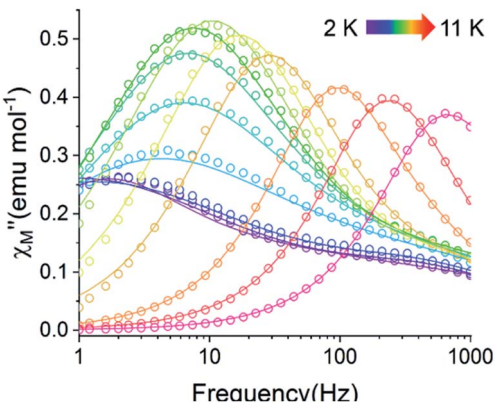


Fig. 9 Temperature dependence of the out-of-phase component of the molar ac magnetic susceptibility ($\chi''_M$) of **2@0.35*T*** ($H = 0.35$ *T*, $T =$ 2–11 K). Lines represent fits to the experimental data (circles).

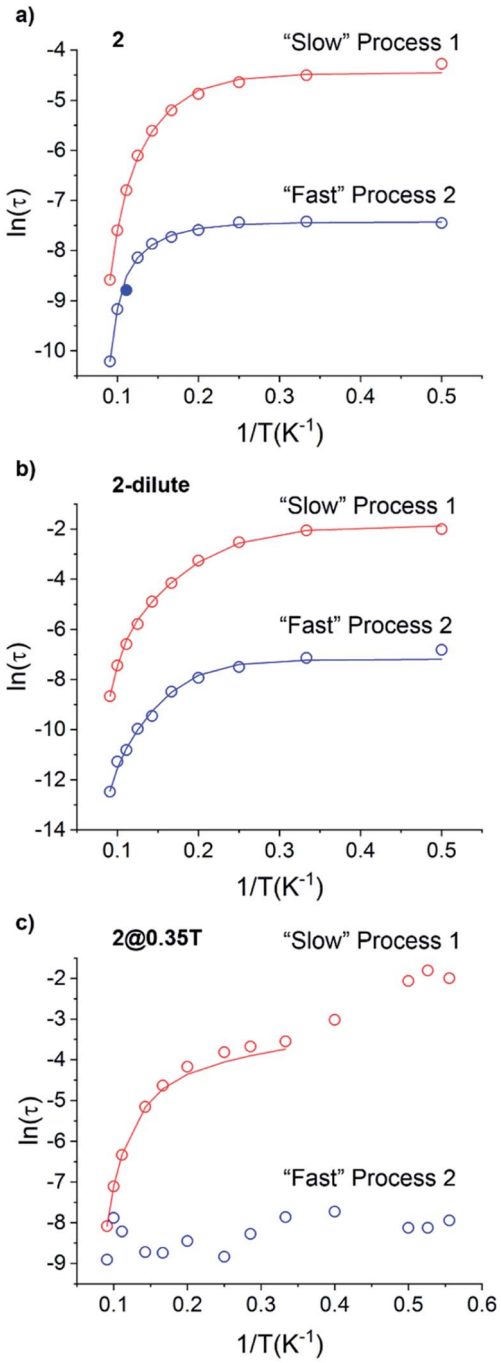


Fig. 10 Arrhenius plots of the magnetic relaxation times of the of the "Slow" and "Fast" magnetic relaxation processes of **2** (a), **2-dilute** (b), and **2@0.35*T*** (c). Solid blue circle in (a) represents point not included in Arrhenius fitting procedure.

low temperatures is still only marginally temperature dependent which might indicate intramolecular phenomenon such as nuclear hyperfine interactions are contributing to the QTM of **2**.

QTM pathways can also be mitigated by creating a field bias upon the application of an external magnetic field which breaks the degeneracy of the $\pm m_j$ crystal field states thereby lowering the probability of spin relaxation through tunneling mechanisms. The temperature dependence of the ac magnetic susceptibility of compound **2** was measured under an optimal 0.35 *T* magnetic field (Fig. S31†) from 1.8–11 K. In an external field, the 2 K $\chi_M''$ signal of **2@0.35*T*** remains broad but shows a significant shift of the maximum to lower frequencies suggesting an increase in the magnetic relaxation time (Fig. 9). Heating the sample to 5 K results in a high frequency shift of the $\chi_M''$ maximum as well as an increase in the magnitude of the signal. Interestingly, heating past 5 K results in an increase in symmetry of the $\chi_M''$ signal and indicates the spin dynamics of **2@0.35*T*** is shifting towards a single relaxation process at higher temperatures. The **2@0.35*T*** magnetic relaxation time for the **SR** process at 2 K of $\tau_1 = 0.13$ s (determined using eqn (1)) is close to the corresponding **SR** process relaxation time for **2-dilute** at the same temperature. This observation suggests application of an external field and magnetic dilution have similar effects on the magnetization dynamics of **2**, at least when considering only the **SR** process.

The magnetic relaxation times extracted using eqn (1) were used to construct Arrhenius plots ($\ln(\tau)$ *vs.* $1/T$) for each of the

Table 2 Arrhenius parameters of **2**, **2-dilute**, and **2@0.35*T*** extracted using eqn (2)

| Compound | **2** | **2@0.35*T*** | **2-dilute** |
|---|---|---|---|
| **Relaxation process 1** | | | |
| $A$ ($S^{-1}$ $T^{-2}$ $K^{-1}$) | | 114 | |
| $\tau_{QTM}$ (s) | 0.0116 | 0 | 0.157 |
| $C$ ($s^{-1}$ $K^{-n}$) | 0.00132 | 0.000261 | 0.00432 |
| $n$ | 4.92 | 6.47 | 5.29 |
| $\tau_o$ (s) | $1.56 \times 10^{-10}$ | $2.88 \times 10^{-11}$ | $2.88 \times 10^{-11}$ |
| $U$ ($cm^{-1}$) | 110 | 129 | 121 |
| **Relaxation process 2** | | | |
| $A$ ($S^{-1}$ $T^{-2}$ $K^{-1}$) | | | |
| $\tau_{QTM}$ (s) | 0.000593 | | 0.000755 |
| $C$ ($s^{-1}$ $K^{-n}$) | 0.251 | | 0.00679 |
| $n$ | 4.25 | | 6.08 |
| $\tau_o$ (s) | $2.02 \times 10^{-12}$ | | $6.21 \times 10^{-13}$ |
| $U$ ($cm^{-1}$) | 131 | | 126 |

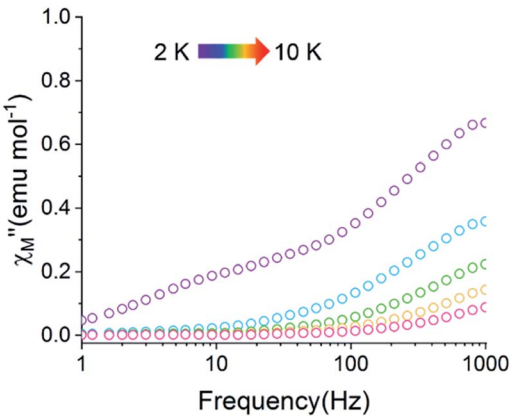


Fig. 11 Temperature dependence of the out-of-phase component of the molar ac magnetic susceptibility ($\chi_M''$) of **2-py** ($H = 0$ *T*, $T = 2$–10 K).

**SR** and **FR** processes of **2**, **2-dilute**, and **2@0.35*T*** (Fig. 10). Each Arrhenius plot was fit using eqn (2), which accounts for spin relaxation through direct, QTM, Raman, and Orbach relaxation processes.[63]

$$\tau^{-1} = AH^{n1}T + {\tau_{QTM}}^{-1} + CT^{n2} + {\tau_o}^{-1}\exp\left(-\frac{U}{k_bT}\right) \quad (2)$$

In the case of **2** and **2-dilute** where $H = 0$ *T*, the direct term $AH^{n1}T$ becomes zero and was therefore disregarded. For **2@0.35*T***, the direct term $A = 114\ S^{-1}\ T^{-2}\ K^{-1}$ was determined by fitting the field dependence of the magnetic relaxation time (Fig. S31†). Due to the complicated nature of the **2@0.35*T*** ac magnetic susceptibility, the low temperature regime (1.8–2.5 K) could not be fit accurately and only the higher temperature regime (3–11 K) of the **SR** process was considered in the Arrhenius fitting procedure. The best fit parameters obtained using this fitting procedure for **2**, **2-dilute**, and **2@0.35*T*** are given in Table 2. It is important to note that the fitting parameters for the **FR** process of **2** and **2-dilute** should only be considered as rough estimates, as the $\chi_M''$ maximum of the resolved signal lies outside of the measured frequency range at higher temperatures. For all fits, the obtained Raman coefficients ($n_2$) are close to the expected range of $n_2 = 5$–7 for a non-Kramers ion.[63] For the **FR** and **SR** processes of **2**, **2-dilute**, and **2@0.35*T*** energy barrier values between $U = 110$–131 $cm^{-1}$ were obtained.

**Dynamic magnetic properties of $[HoFc_3(py)_2Li_2]^-$ (2-py) and $[HoFc_3(THF^*)_2Li_2]^-$ (2-THF*).** Small perturbations in the crystal-field environment can greatly influence the electronic structure and thus the magnetization dynamics of lanthanide-based molecules. In order to explore how small distortions in the trigonal prismatic $[Fc_3]^{6-}$ ligand field effects the SMM properties of the Ho-[1]ferrocenophane compound, $[HoFc_3(THF)_2Li_2]^-$, the static and dynamic magnetic properties of the pyridine solvated complex, $[HoFc_3(py)_2Li_2]^-$ (**2-py**) were explored.

The static magnetic behavior of **2-py** is nearly identical to that of compound **2** (Fig. S11†). Interestingly, the dynamic magnetic properties of **2-py** are markedly different from that of compound **2** (Fig. 11). Compound **2-py** features extremely broad signals in the $\chi_M''$ *vs.* frequency plot but does not feature any discernable signal maxima within the measured 1–1000 Hz frequency range. This qualitative observation readily suggests that the magnetic relaxation times for the more geometrically distorted Ho-[1]ferrocenophane molecules in **2-py**, are much faster than the magnetic relaxation times observed for the Ho-[1]ferrocenophane molecules in **2**, which features a low frequency $\chi_M''$ signal maximum at 18.2 Hz at 2 K. Upon increasing the temperature above 2 K, the $\chi_M''$ signal of **2-py** moves out of the high frequency limit and almost completely disappears at 10 K. Out-of-phase signals at only the highest frequencies without signal maxima within the frequency range could suggest QTM is a major contributor to the spin relaxation in **2-py**. Although the magnetic relaxation of **2-py** is too fast to allow the extraction of an energy barrier of magnetization reversal, the presented data suggests that the deviation from idealized trigonal prismatic geometry (increase in torsion angle) increases relaxation times.

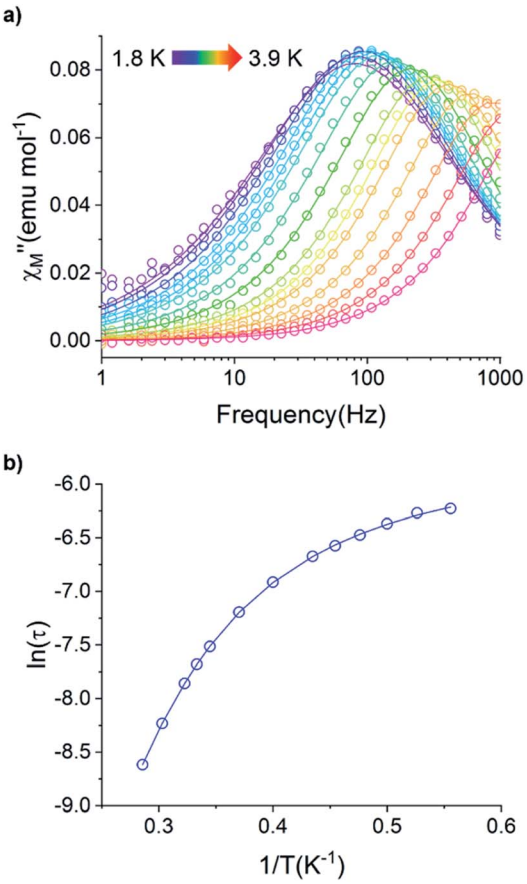


Fig. 12 (a) Temperature dependence of the out-of-phase component of the molar ac magnetic susceptibility ($\chi_M''$) of **5**. ($H = 0.2$ *T*, $T = 1.8$–3.9 K). (b) Arrhenius plot of the magnetic relaxation time of **5**.

Table 3 Energies ($cm^{-1}$) of the lowest energy doublets of **Ln(1)** in **2**–**5**

| Compound | | | |
|---|---|---|---|
| **2** | **3** | **4** | **5** |
| 0 | 0 | 0 | 0 |
| 0.1325 | 52.3575 | 86.9322 | 122.7001 |
| 137.0824 | 133.0082 | 115.6344 | 475.9593 |
| 137.1925 | 151.2557 | 348.8809 | 1208.0192 |
| 227.7217 | 372.2061 | 359.4642 | 10 479.2524 |
| 228.2524 | 433.3370 | 614.8964 | 10 636.9361 |
| 389.3542 | 603.7203 | 628.4261 | 11 490.9949 |
| 390.5907 | — | 793.9510 | |
| 424.9725 | | 794.4556 | |
| 433.2938 | | 912.2663 | |
| 447.0406 | | 912.3256 | |
| 504.8665 | | 1196.5839 | |
| 516.2164 | | 1196.5971 | |
| 522.8741 | | 6103.0014 | |
| 537.9741 | | 6106.8661 | |
| 540.7899 | | | |
| 565.8972 | | | |
| — | | | |

**Dynamic magnetic properties of $[LnFc_3(THF)_2Li_2]^-$ (Ln = $Er^{3+}$ (3), $Tm^{3+}$ (4), and $Yb^{3+}$ (5)).** For the $Er^{3+}$, $Tm^{3+}$, and $Yb^{3+}$ compounds **3**, **4**, and **5** respectively, no appreciable signal is observed in the $\chi''_M$ *vs.* Frequency plot in the absence of an external magnetic field. This result is not surprising as the axial $[LnFc_3]^{3-}$ ligand field likely destabilizes the largest $m_j = \pm 15/2$, $\pm 6$, and $\pm 7/2$ projections of the prolate $Er^{3+}$, $Tm^{3+}$, and $Yb^{3+}$ ions, respectively. These results are also consistent with dc magnetization data for the $Tm^{3+}$ compounds, **4**, which suggest the lowest energy $m_j = 0$ ground state for **4**.

For the $Yb^{3+}$ compound $\mathbf{5/5^{Iso}}$, application of an optimal 0.2 T external magnetic field results in slow magnetic relaxation behavior as evidenced by a narrow temperature dependent signal in $\chi''_M$ *vs.* Frequency plot (Fig. 12a). Between 1.8–2 K, the magnitude of the $\chi''_M$ signal increases which could suggest that the spin relaxation is occurring through multiple relaxation mechanisms at the lowest temperatures and subsequently shifting towards a single mechanism upon heating. Heating results in an increased temperature dependence of the $\chi''_M$ single maximum which eventually moves outside of the measured frequency range at 3.5 K.

Using the ac magnetic susceptibility of compound $\mathbf{5/5^{Iso}}$, Cole–Cole curves were constructed and were fitted using general Debye equation which considers only one spin relaxation process. The extracted magnetic relaxation times were then used to construct an Arrhenius plot between 1.8–3.5 K (Fig. 12b). Analyzing the Arrhenius plot for compound **5** shows the magnetic relaxation times for **5** are temperature dependent across the full temperature range suggesting low contribution from quantum tunneling processes. Between 2.5–3.5 K, the magnetic relaxation times become increasingly temperature dependent but never become fully linear on the logarithmic scale. This indicates significant contributions to the spin relaxation from second-order Raman and/or direct processes even at the highest temperature regime. Similar behavior has been observed in the trigonal $Yb^{3+}$ SMM, Yb[trensal], where it was reported that considering solely an Orbach relaxation mechanism was insufficient in describing the anisotropy energy barrier of the system.[64] As previously described, the Arrhenius plot for $\mathbf{5/5^{Iso}}$ was fit using eqn (2). The direct exponent, $n_1$, was held constant at $n_1 = 4$ and the direct term, $A$, was allowed to freely refine along with the other Arrhenius parameters due to the inability in acquiring a reasonable fit of the $\tau$ *vs.* H plot for compound $\mathbf{5/5^{Iso}}$ (Fig. S49†). Using this fitting procedure, values of Arrhenius parameters of $A = 0.304\ S^{-1}\ T^{-2}\ K^{-1}$, $\tau_{QTM} = 0.00269$ s, $C = 0.00812\ s^{-1}\ K^{-4}$,[25] $n_2 = 4.25$, $\tau_o = 9.04 \times 10^{-5}$ s, and $U = 6\ cm^{-1}$ were obtained.

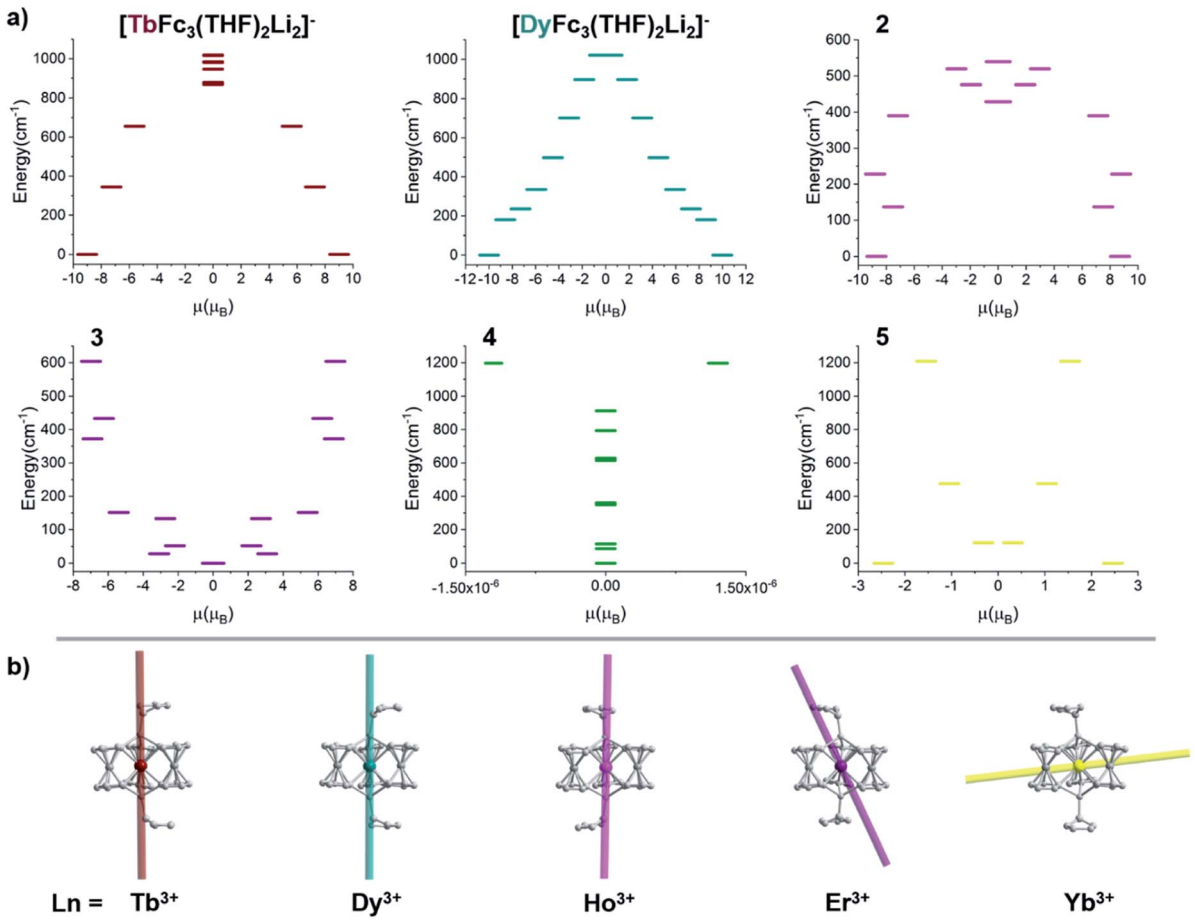


Fig. 13 (a) Ground state electronic structure of compounds $[TbFc_3Li_2(THF)_2]^-$, $[DyFc_3Li_2(THF)_2]^-$, and **2**–**5**. (b) Depiction of the magnetic anisotropy axis of $[TbFc_3Li_2(THF)_2]^-$, $[DyFc_3Li_2(THF)_2]^-$, **2**, **3**, and **5**.

 

### Electronic structure determination of compounds 1–5

To further investigate the electronic structure of the late lanthanide ions in the trigonal prismatic geometry and the observed magnetic properties of **2–5**, multi-configurational *ab initio* calculations were performed using the Molcas 8.2 package within the CASSCF/SO-RASSI and XMS-CASPT2/SO-RASSI level of theory.[65] For the two independent **Ln(1)** and **Ln(2)** molecules of **2–5**, there are only small differences of the energies of the spin–orbit states and corresponding *g*-tensors, therefore only the results obtained for **Ln(1)** within the XMS-CASPT2 level of theory will be discussed here (Tables S21–S27†) (Table 3).

The ground state electronic structures for **2–5** are shown in Fig. 13. The axial nature of the trigonal prismatic ligand field is expected to be least suitable for stabilizing the largest $m_j$ projections in the latest prolate lanthanide ions ($Er^{3+}$, $Tm^{3+}$, and $Yb^{3+}$). The Er-[1]ferrocenophane compound, **3**, shows highly mixed ground doublets containing $m_j = \pm 1/2$ (24%), $\pm 5/2$ (23%), and $\pm 7/2$ (18.7%) character. The first and second excited $m_j$ states for **3** reside only 28 $cm^{-1}$ and 52 $cm^{-1}$ above the ground doublets which contributes to the highly mixed $m_j$ composition and large transverse *g*-tensors ($g_x$ and $g_y$) of **3** (Table 4). These factors contribute to the lack of axial magnetic anisotropy of the ground state and explain the lack of SMM behavior for **3**. For compound **4**, a non-magnetic, $m_j = 0$, ground state is observed and therefore it does not exhibit any magnetic anisotropy. This corresponds well with the direct current magnetic susceptibility data in which the molar magnetic susceptibility temperature product drops to near zero at 2 K. The composition of the ground doublet of the Yb-[1] ferrocenophane compound, **5**, is mostly $m_j = \pm 7/2$ (51%) and $\pm 3/2$ (11%) character and exhibits large transversal *g*-tensors which leads to a magnetic anisotropy axis which is nearly perpendicular to the principal $C_3$ axis of the $[LnFc_3(THF)_2Li_2]^-$ motif. Therefore, the lack of SMM behavior of **5** in the absence of an external magnetic field is not surprising as fast spin relaxation through QTM processes is expected. To this end, the observed slow relaxation under an applied magnetic field suggests that the ground $m_j = \pm 7/2$ doublet becomes purer under an applied field and therefore QTM is at least partially shut down. For **5**, the first excited $m_j$ state lies 121 $cm^{-1}$ above the ground doublet, therefore if the spin relaxation of **5** under an applied field proceeds *via* an Orbach mechanism through the first excited state, and energy barrier ~120 $cm^{-1}$ is likely to be observed under an applied magnetic field. The experimentally extracted spin reversal barrier of 6 $cm^{-1}$ is significantly lower than the energy gap between the ground and first excited state and suggest that spin relaxation proceeds mainly through a second-order Raman and/or direct mechanism.

Table 4 The g-tensor of the lowest four doublets of Ln(1) in **2–5**

| Doublet | | Compound **2** | **3** | **4** | **5** |
|---|---|---|---|---|---|
| 1 | $g_x$ | 0 | 9.997 | — | 1.847 |
| | $g_y$ | 0 | 7.516 | — | 2.645 |
| | $g_z$ | 17.400 | 0.150 | — | 4.920 |
| 2 | $g_x$ | 0 | 2.156 | — | 0.425 |
| | $g_y$ | 0 | 4.736 | — | 0.677 |
| | $g_z$ | 15.025 | 8.965 | — | 6.893 |
| 3 | $g_x$ | 0 | 4.983 | — | 0.042 |
| | $g_y$ | 0 | 3.382 | — | 0.336 |
| | $g_z$ | 17.774 | 0.736 | — | 5.298 |
| 4 | $g_x$ | 0 | 10.797 | — | 0.084 |
| | $g_y$ | 0 | 6.514 | — | 0.087 |
| | $g_z$ | 14.354 | 1.797 | — | 7.987 |

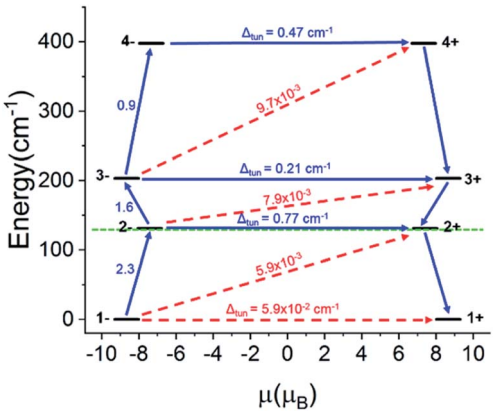


Fig. 14 Calculated barrier for magnetization reversal for Ho(2). The doublet states are arranged according to the values of their magnetic moments. The numbers at each arrow show the corresponding matrix element of the transversal magnetic moment, whereas $\Delta_{tun}$ is the intrinsic tunneling gap of the corresponding doublet.

For the Ho-[1]ferrocenophane compound, **2**, an almost pure $m_j = \pm 7$ ground state is observed and is well stabilized from the first and second excited states by 137 $cm^{-1}$ and 228 $cm^{-1}$, respectively. The highly anisotropic ground state leads to an axial magnetic moment vector that resides along the principal {$LnFc_3$} $C_3$ axis explaining the observed SMM behavior of **2**. The magnetic blocking barrier of the **Ho(2)** molecule of **2** was further investigated by following the methodology described in ref. 66 (Fig. 14). The tunneling gaps between the ground doublets are small which suggests ground state QTM is minimal. Spin relaxation is expected to proceed through the first excited state given the large tunneling gap of 0.77 $cm^{-1}$. The energy of the first excited state (137 $cm^{-1}$) corresponds remarkably well with the experimentally extracted energy barriers of **2**, **2-dilute**, and **2@0.35*T*** (110–131 $cm^{-1}$).

## Conclusions

We present a detailed analysis of trends in structure and magnetic properties of the remaining members of the family of late Ln-[1]ferrocenophane complexes which all feature exclusively carbon-donors coordinated to trigonal prismatic lanthanide ions. The observed trend of increasing $Fc^{2-}$ twist angle with decreasing ionic radii of the $Ln^{3+}$ ions can be rationalized by simple geometric arguments and considering the structural rigidity of the $Fc^{2-}$ units. The $Ho^{3+}$ complex **2** exhibits slow magnetic relaxation in the absence of applied dc fields, rendering it a rare example of a $Ho^{3+}$-based SMM. Structural

modification of the approximate trigonal prismatic coordination environment can be achieved remotely *via* substitution of coordinating solvent molecules to the terminating $Li^+$ ions. Specifically, an increase in $Fc^{2-}$ twist angle and deviation from ideal trigonal prismatic geometry is observed in the series **2**, **2-THF***, and **2-py** which is accompanied by a decrease in magnetic relaxation times at a given temperature for the pyridine solvated molecule **2-py**. Taken together our results emphasize the sensitivity of the magnetic structure of $Ln^{3+}$ ions in trigonal prismatic coordination environments to the twist angle and provide design guidelines for six-coordinate SMMs.

# Experimental section

### General materials and methods

All syntheses and magnetic sample preparation were carried out under the rigorous exclusion of air and moisture using an ultra-high purity Ar filled glovebox (Vigor) in which the $O_2$ and $H_2O$ levels were generally held under 2 ppm and 0.1 ppm, respectively. Tetrahydrofuran, diethyl ether, hexanes, and *n*-pentane were all dried and deoxygenated using a solvent purification system (JC Meyer or Innovative Technologies SPS) and were stored over molecular sieves (**3a**, 8 to 12 mesh) prior to use. Pyridine was dried by stirring over $CaH_2$ for 24 hours and deoxygenated using freeze–pump–thaw methods. Prior to use 2-methyl tetrahydrofuran (THF*) was passed through a basic alumina column to remove the butylated hydroxytoluene (BHT) stabilizer. Stabilizer free THF* was deoxygenated by purging $N_2$ gas through the solvent and was dried by refluxing over Na/benzophenone. Anhydrous THF* and pyridine were stored over molecular sieves (**3a**, 8 to 12 mesh). Anhydrous $GdCl_3$, $HoCl_3$, and $ErCl_3$ were received as a generous gift from Dr Timothy Hughbanks. Anhydrous $TmCl_3$ (Millipore Sigma), $YbCl_3$ (Alfa Aesar), and $LuCl_3$ (Alfa Aesar) were purchased from commercial sources and were used as received. $Li_6(Fe(\eta^5\text{-}C_5H_4)_2)_3(TMEDA)_2$ (ref. 67) and $[Li(THF)_4][YFc_3(THF)_2Li_2]$[44] were prepared as previously described. Carbon and hydrogen elemental analysis were performed on compounds **1–6**, and **2-py** by Midwest Microlab Inc.

### X-ray crystallography

Details regarding the structural determination of compounds **1–6**, $\mathbf{5^{Iso}}$, $\mathbf{6^{Iso}}$, **2-THF***, and **2-py** can be found in the ESI.†

### Magnetic characterization

Samples used for magnetic characterization were prepared by thoroughly crushing the respective paramagnetic species into a microcrystalline powder and subsequently adding between 20–40 mg to the bottom of a high purity glass NMR tube along with solid *n*-eicosane (~27–65 mg). The NMR tube containing the paramagnetic species/*n*-eicosane mixture was equipped with a gas line adaptor, removed from the glovebox, and was sealed under vacuum on a Schlenk line. To prevent torqueing of small crystallites under high magnetic fields, the solid *n*-eicosane in the sealed sample was melted by heating the sealed tube between 40–43 °C in a hot water bath, forming a solid matrix upon cooling to room temperature.

Magnetic characterization was carried out using a Quantum Design MPMS 3 SQUID magnetometer. The direct current (dc) magnetic susceptibility was measured under a 0.1 *T* magnetic field between 2–300 K. A diamagnetic correction (calculated using Pascal's constants) was included in the calculation of the dc molar magnetic susceptibility and considers the diamagnetic response of eicosane and the complex core electrons.[68] The variable temperature magnetization was measured between 2–8 K up to external magnetic field strengths of 7 *T*. The alternating current (ac) magnetic susceptibly was measured using a 0.2 mT alternating field between 1–1000 Hz using external field strengths of either 0 T, 0.2 *T*, or 0.35 *T*.

### Synthesis

**$[Li(THF)_4][GdFc_3(THF)_2Li_2]$ (1).** A 20 mL vial was charged with $GdCl_3$ (0.1590 g; 0.6032 mmols), THF (2 mL), and a magnetic stir bar. The suspension was heated to 45 °C and stirred vigorously for *ca.* 8 hours. The suspension was then added to a vial containing a suspension of $Li_6(Fe(C_5H_4)_2)_3$(-TMEDA)$_2$ (0.6618 g; 0.8011 mmols) in THF (5–10 mL), stirred with a glass coated stir bar, forming a cloudy red suspension. The suspension was let stir for 16–18 hours upon which the reaction mixture was filtered through Celite. The dark red filtrate was reduced under dynamic vacuum forming a viscid oil which expanded as a sticky solid upon agitation. The red-orange solid was washed with hexanes (4 × 5 mL) and was subsequently dried under vacuum to yield a light orange powder. The crude product was extracted into several washings of $Et_2O$ (4 × 5 mL) which were filtered through Celite. The $Et_2O$ filtrate was reduced to dryness under dynamic vacuum and the resulting orange material was dissolved in THF (3–5 mL), filtered through Celite, and placed into a pentane vapor diffusion chamber. Pyrophoric plate crystals of 1 formed overnight at −27 °C, which were collected by decantation of the mother liquor, washing with pentane (2 × 2 mL), and allowing the crystals to dry under an Ar atmosphere at ambient temperature and pressure (0.2166 g; yield = 31.96%). *In contrast to compounds **2–6** and **2-py**, elemental analysis on crystalline material of **1** using commercial analysis services resulted in low C and H values. This discrepancy could be due to the smaller crystals obtained for **1** and resulting increased propensity for desolvation of THF molecules or product decomposition prior to analysis.

**$[Li(THF)_4][HoFc_3(THF)_2Li_2]$ (2).** To a 20 mL vial containing $Li_6(Fe(C_5H_4)_2)_3(TMEDA)_2$ (0.4559 g; 0.552 mmols) in THF (5–10 mL) was added solid $HoCl_3$ (0.1117 g; 0.412 mmols) and an additional THF wash (4–5 mL) forming a red suspension. The suspension was let stir for 16–18 hours upon which the reaction mixture was filtered through Celite. The dark red filtrate was reduced under dynamic vacuum forming a viscid oil which expanded as a sticky solid upon agitation. The red-orange solid was washed with hexanes (3 × 5 mL) and was subsequently dried under vacuum to yield a light orange powder. The crude product was extracted into several washings of $Et_2O$ (4 × 5 mL) which were filtered through Celite. The $Et_2O$ filtrate was

 

reduced to dryness under dynamic vacuum and the resulting orange material was dissolved in THF (3–5 mL), filtered through Celite, and placed into a pentane vapor diffusion chamber. Large pyrophoric plate crystals of **2** formed overnight at −27 °C, which were collected by decantation of the mother liquor, washing with pentane (2 × 2 mL), and allowing the crystals to dry under an Ar atmosphere at ambient temperature and pressure (0.2555 g; yield = 40.46%) Anal. calcd for $C_{54}H_{72}Fe_3HoLi_3O_6$ (found): C, 55.41 (55.11); H, 6.20 (5.89).

**$[Li(Py)_4][HoFc_3(Py)_2Li_2]$ (2-py).** $[Li(THF)_4][HoFc_3(THF)_2Li_2]$ (0.0475 g; 0.0406 mmols) was dissolved in pyridine (1–2 mL) forming an orange solution. The solution was filtered through Celite and placed in a vapor diffusion chamber using pentanes as the volatile. Red plate crystals of **2-py** grew over several days at −27 °C and were collected by decanting the mother liquor, washing with pentane (2 × 2 mL), and allowing the crystals to dry under an Ar atmosphere at ambient temperature and pressure (yield: 0.0165 g; 31.7%). Anal. calcd. for $C_{64.38}H_{58.38}Fe_3HoLi_3N_{6.88}$ (found): C, 60.33 (59.29); H, 4.59 (4.54); N, 7.52 (6.62). Anal. calcd. for $C_{59.38}H_{53.38}Fe_3HoLi_3N_{5.88}$ (found): C, 59.30 (59.29); H, 4.47 (4.54); N, 6.85 (6.62).

**$[Li(THF^*)_4][HoFc_3(THF^*)_2Li_2]$ (2-THF*).** $[Li(THF)_4][HoFc_3(THF)_2Li_2]$ (0.1045 g; 0.08928 mmols) was dissolved in 2-methyl THF (2–3 mL) forming an orange solution. The solution was filtered through Celite and placed in a vapor diffusion chamber using pentanes as the volatile. Red plate crystals of **2-THF*** along with small amount of orange plates of different morphology grew over 3–4 days at −27 °C and were collected by decanting the mother liquor, washing with pentane (2 × 2 mL), and allowing the crystals to dry under an Ar atmosphere at ambient temperature and pressure (yield: 0.0838 g; 74.8%). Due to small amounts of an impurity, apparent *via* X-ray crystallography, elemental analysis was not attempted for **2-THF***.

**$[Li(THF)_4][Ho_{0.06}Y_{0.94}Fc_3(THF)_2Li_2]$ (2-dilute).** $[Li(THF)_4][HoFc_3(THF)_2Li_2]$ (0.0025 g; 0.0021 mmols) and $[Li(THF)_4][YFc_3(THF)_2Li_2]$ (0.0353 g; 0.0323 mmols) were weighed in separate vials. $[Li(THF)_4][YFc_3(THF)_2Li_2]$ was completely dissolved in THF (2 mL) and the resulting solution was added to solid $[Li(THF)_4][HoFc_3(THF)_2Li_2]$ along with an additional THF wash (1 mL). Upon complete dissolution of $[Li(THF)_4][HoFc_3(THF)_2Li_2]$, the solution was placed in a pentane 2-dilute grew overnight. The crystals were collected by decantation of the mother liquor, washing with pentane (2 × 2 mL), and allowing the crystals to dry under an Ar atmosphere ambient temperature and pressure (0.0245 g; yield = 65%). Unit cell (110 K): $a$ = 11.40 Å; $b$ = 63.59 Å; $c$ = 13.74 Å; $\alpha$ = 90.00°; $\beta$ = 92.26°; $\lambda$ = 90.00°; volume = 9951 Å$^3$.

**$[Li(THF)_4][ErFc_3(THF)_2Li_2]$ (3).** Synthesis analogous to preparation of **2** using $ErCl_3$ (0.101 g; 0.370 mmols) and $Li_6(Fe(C_5H_4)_2)_3(TMEDA)_2$ (0.407 g; 0.492 mmols) (0.1957 g; yield = 50.07%). Anal. calcd for $C_{54}H_{72}Fe_3ErLi_3O_6$ (found): C, 55.30 (55.03); H, 6.19 (6.06).

**$[Li(THF)_4][TmFc_3(THF)_2Li_2]$ (4).** Synthesis analogous to preparation of **1** using $TmCl_3$ (0.0930 g; 0.338 mmols) and $Li_6(Fe(C_5H_4)_2)_3(TMEDA)_2$ (0.3719 g; 0.04502 mmols) (0.2227 g; yield = 91.47%). Anal. calcd for $C_{54}H_{72}Fe_3TmLi_3O_6$ (found): C, 55.22 (55.19); H, 6.18 (6.33).

**$[Li(THF)_4][YbFc_3(THF)_2Li_2]$ (5, $5^{Iso}$).** Synthesis analogous to preparation of **1** using $YbCl_3$ (0.1416 g; 0.5068 mmols) and $Li_6(Fe(C_5H_4)_2)_3(TMEDA)_2$ (0.5565 g; 0.6736 mmol). Large plate crystals of **5** along with a smaller amount of brown rod crystals of $\mathbf{5^{Iso}}$ apparent in product mixture (0.124 g; yield = 20.7% using theoretical yield for pure 5) Anal. calcd for $C_{54}H_{72}Fe_3YbLi_3O_6$ (found): C, 55.03 (54.90); H, 6.16 (6.19).

**$[Li(THF)_4][LuFc_3(THF)_2Li_2]$ (6, $6^{Iso}$).** Synthesis analogous to preparation of **5** and $\mathbf{5^{Iso}}$ using $LuCl_3$ (0.1311 g; 0.4660 mmols) and $Li_6(Fe(C_5H_4)_2)_3(TMEDA)_2$ (0.5132 g; 0.6212 mmols) (0.1496 g; yield = 27.20% using theoretical yield for pure 6) $^1$H NMR (400 MHz, THF-$d_8$): $\delta$(ppm) 4.05 (s, 4H, $C_5H_4$) 4.09 (s, 4H, $C_5H_4$) Anal. calcd for $C_{54}H_{72}Fe_3LuLi_3O_6$ (found): C, 54.94 (55.39); H, 6.15 (6.02).

## Conflicts of interest

There are no conflicts to declare.

## Acknowledgements

M. N. is grateful for support of this project by the National Science Foundation (CHE-1753014) and general financial support through The Welch Foundation (A-1880). V. V. acknowledges the postdoctoral fellowships from the Fonds Wetenschappelijk Onderzoek Vlaanderen (FWO, Flemish Science Foundation). A. U. is grateful to SERB/IUSSTF (India) for a postdoctoral fellowship. We thank Dr Timothy Hughbanks for the generous gift of anhydrous lanthanide salt starting materials.

## Notes and references

1 D. Gatteschi, R. Sessoli and J. Villain, *Molecular Nanomagnets*, Oxford Univ. Press., 2006.
2 M. Mannini, F. Pineider, C. Danieli, F. Totti, L. Sorace, P. Sainctavit, M. A. Arrio, E. Otero, L. Joly, J. C. Cezar, A. Cornia and R. Sessoli, *Nature*, 2010, **468**, 417–421.
3 M. Mannini, F. Pineider, P. Sainctavit, C. Danieli, E. Otero, C. Sciancalepore, A. M. Talarico, M. A. Arrio, A. Cornia, D. Gatteschi and R. Sessoli, *Nat. Mater.*, 2009, **8**, 194–197.
4 P. C. Bunting, M. Atanasov, E. Damgaard-Møller, M. Perfetti, I. Crassee, M. Orlita, J. Overgaard, J. van Slageren, F. Neese and J. R. Long, *Science*, 2018, **362**, eaat7319.
5 X. Yao, J. Du, Y. Zhang, X. Leng, M. Yang, S. Jiang, Z. Wang, Z. Ouyang, L. Deng, B. Wang and S. Gao, *J. Am. Chem. Soc.*, 2017, **139**, 373–380.
6 J. M. Zadrozny, D. J. Xiao, M. Atanasov, G. J. Long, F. Grandjean, F. Neese and J. R. Long, *Nat. Chem.*, 2013, **5**, 577–581.
7 K. L. M. Harriman, J. L. Brosmer, L. Ungur, P. L. Diaconescu and M. Murugesu, *J. Am. Chem. Soc.*, 2017, **139**, 1420–1423.
8 Y. Ding, N. F. Chilton, R. E. P. Winpenny and Y. Zheng, *Angew. Chem., Int. Ed.*, 2016, **55**, 16071–16074.
9 M. Gregson, N. F. Chilton, A. Ariciu, F. Tuna, I. F. Crowe, W. Lewis, A. J. Blake, D. Collison, E. J. L. McInnes,

R. E. P. Winpenny and S. T. Liddle, *Chem. Sci.*, 2016, **7**, 155–165.
10 Y. Chen, J. Liu, L. Ungur, J. Liu, Q. Li, L. Wang, Z. Ni, L. F. Chibotaru, X.-M. Chen and M.-L. Tong, *J. Am. Chem. Soc.*, 2016, **138**, 2829–2837.
11 N. Ishikawa, M. Sugita, T. Ishikawa, S. Koshihara and Y. Kaizu, *J. Am. Chem. Soc.*, 2003, **125**, 8694–8695.
12 P. Evans, D. Reta, G. F. S. Whitehead, N. F. Chilton and D. P. Mills, *J. Am. Chem. Soc.*, 2019, **141**, 19935–19940.
13 C. A. Gould, K. R. McClain, J. Yu, T. J. Groshens, F. Furche, J. R. Long and B. G. Harvey, *J. Am. Chem. Soc.*, 2019, **141**, 12967–12973.
14 K. R. McClain, C. A. Gould, K. Chakarawet, S. J. Teat, T. J. Groshens, J. R. Long and B. G. Harvey, *Chem. Sci.*, 2018, **9**, 8492–8503.
15 F.-S. Guo, B. M. Day, Y.-C. Chen, M.-L. Tong, A. Mansikkamaki and R. A. Layfield, *Science*, 2018, **362**, 1400–1403.
16 B. M. Day, F.-S. Guo and R. A. Layfield, *Acc. Chem. Res.*, 2018, **51**, 1880–1889.
17 C. A. P. Goodwin, F. Ortu, D. Reta, N. F. Chilton and D. P. Mills, *Nature*, 2017, **548**, 439–442.
18 F.-S. Guo, B. M. Day, Y.-C. Chen, M.-L. Tong, A. Mansikkamaki and R. A. Layfield, *Angew. Chem., Int. Ed.*, 2017, **56**, 11445–11449.
19 D. N. Woodruff, R. E. P. Winpenny and R. A. Layfield, *Chem. Rev.*, 2013, **113**, 5110–5148.
20 J. D. Rinehart and J. R. Long, *Chem. Sci.*, 2011, **2**, 2078–2085.
21 D. Gatteschi and R. Sessoli, *Angew. Chem., Int. Ed.*, 2003, **42**, 268–297.
22 J. Wu, J. Jung, P. Zhang, H. Zhang, J. Tang and B. L. Guennic, *Chem. Sci.*, 2016, **7**, 3632–3639.
23 A. Watanabe, A. Yamashita, M. Nakano, T. Yamamura and T. Kajiwara, *Chem.–Eur. J.*, 2011, **17**, 7428–7432.
24 S. Jiang, B. Wang, G. Su, Z. Wang and S. Gao, *Angew. Chem., Int. Ed.*, 2010, **49**, 7448–7451.
25 Y. Chen, F. Ma, X. Chen, B. Dong, K. Wang, S. Jiang, C. Wang, X. Chen, D. Qi, H. Sun, B. Wang, S. Gao and J. Jiang, *J. Inorg. Chem.*, 2017, **56**, 13889–13896.
26 C. R. Ganivet, B. Balleseros, G. de la Torre, J. M. Clemente-Juan, E. Coronado and T. Torres, *Chem.–Eur. J.*, 2012, **19**, 1457–1465.
27 S. Takamatsu, T. Ishikawa, S. Koshihara and N. Ishikawa, *Inorg. Chem.*, 2007, **46**, 7250–7252.
28 M. A. AlDaman, S. Cardonna-Serra, J. M. Clemente-Juan, E. Coronado, A. Gaita-Ariño, C. Martí-Gastaldo, F. Luis and O. Montero, *Inorg. Chem.*, 2009, **48**, 3467–3479.
29 M. A. AlDaman, J. M. Clemente-Juan, E. Coronado, C. Martí-Gastaldo and A. Gaita-Ariño, *J. Am. Chem. Soc.*, 2008, **130**, 8874–8875.
30 S. K. Gupta, T. Rajeshkumar, G. Rajaraman and R. Murugavel, *Chem. Sci.*, 2016, **7**, 5181–5191.
31 J. Liu, Y. Chen, J. Liu, V. Vieru, L. Ungur, J. Jia, L. F. Chibotaru, Y. Lan, W. Wernsdorfer, S. Gao, X. Chen and M. Tong, *J. Am. Chem. Soc.*, 2016, **138**, 5441–5450.
32 Y. S. Meng, C. H. Wang, T. Q. Zhang, X. B. Leng, B. W. Wang, Y. F. Chen and S. Gao, *Inorg. Chem. Front.*, 2016, **3**, 828–835.
33 J. J. Le Roy, I. Korobkov and M. Murugesu, *Chem. Commun.*, 2014, **50**, 1602–1604.
34 K. R. Miehaus and J. R. Long, *J. Am. Chem. Soc.*, 2013, **135**, 17952–17957.
35 S. Jiang, B. Wang, H. Sun, X. Wang and S. Gao, *J. Am. Chem. Soc.*, 2011, **133**, 4730–4733.
36 M. Guo and J. Tang, *Inorganics*, 2018, **6**, 16.
37 S. Liu, Y. Meng, Y. Zhang, Z. Meng, K. Lang, Z. Zhu, C. Shang, B. Wang and S. Gao, *Inorg. Chem.*, 2017, **56**, 7320–7323.
38 B. Na, X. Zhang, W. Shi, Y. Zhang, B. Wang, X. Gao, S. Gao and P. Cheng, *Chem.–Eur. J.*, 2014, **20**, 15975–15980.
39 K. R. Miehaus, J. D. Rinehart and J. R. Long, *Inorg. Chem.*, 2011, **50**, 8484–8489.
40 K. R. Miehaus, S. G. Minasian, W. W. Lukens Jr, S. A. Kozimor, D. K. Shuh, T. Tyliszczak and J. R. Long, *J. Am. Chem. Soc.*, 2014, **136**, 6056–6068.
41 L. Ungur and L. F. Chibotaru, *Inorg. Chem.*, 2016, **55**, 10043–10056.
42 R. A. Layfield and M. Murugesu, *Lanthanides and Actinides in Molecular Magnetism*, John Wiley & Sons, Weinheim, Germany, 2015.
43 J. J. Baldoví, S. Cardonna-Serra, J. M. Clemente-Juan, E. Coronado, A. Gaita-Ariño and A. Palii, *Inorg. Chem.*, 2012, **51**, 12565–12574.
44 T. P. Latendresse, N. S. Bhuvanesh and M. Nippe, *J. Am. Chem. Soc.*, 2017, **139**, 8058–8061.
45 T. P. Latendresse, V. Vieru, B. O. Wilkins, N. S. Bhuvanesh, L. F. Chibortaru and M. Nippe, *Angew. Chem., Int. Ed.*, 2018, **57**, 8164–8169.
46 R. D. Shannon, *Acta Crystallogr., Sect. A: Cryst. Phys., Diffr., Theor. Gen. Crystallogr.*, 1976, **32**, 751–767.
47 M. Shiddiq, D. Komijani, Y. Duan, A. Gaita-Ariño, E. Coronado and S. Hill, *Nature*, 2016, **531**, 348–351.
48 N. F. Chilton, *Inorg. Chem.*, 2015, **54**, 2097–2099.
49 R. Olejník, Z. Padělková, A. Fridrichová, M. Horáček, J. Merna and A. Růžička, *J. Organomet. Chem.*, 2014, **759**, 1–10.
50 A. Caralho, A. Domingos, P. Gaspar, N. Marques, A. Piresde Matos and I. Santos, *Polyhedron*, 1992, **11**, 1481–1488.
51 Unpublished results.
52 Y. Chen, J. Liu, W. Wernsdorfer, D. Liu, L. F. Chibotaru, X. Chen and M. Tong, *Angew. Chem., Int. Ed.*, 2017, **56**, 4996–5000.
53 J. Dreiser, R. Westerström, Y. Zhang, A. A. Popov, L. Dunsch, K. Krämer, X. Liu, S. Decurtins and T. Greber, *Chem.–Eur. J.*, 2014, **20**, 13536–13540.
54 S. Cardona-Serra, J. M. Clemente-Juan, E. Coronado, A. Gaita-Ariño, A. Camón, M. Evangelisti, F. Luis, M. J. Martínez-Pérez and J. Sesé, *J. Am. Chem. Soc.*, 2012, **134**, 14982–14990.
55 J. D. Rinehart, M. Fang, W. J. Evans and J. R. Long, *J. Am. Chem. Soc.*, 2011, **133**, 14236–14239.
56 R. J. Blagg, F. Tuna, E. J. L. McInnes and R. E. P. Winpenny, *Chem. Commun.*, 2011, **47**, 10587–10589.
57 N. Isikawa, M. Sugita and W. Wernsdorfer, *J. Am. Chem. Soc.*, 2005, **127**, 3650–3651.

 

58 C. A. P. Goodwin, D. Reta, F. Ortu, N. F. Chilton and D. P. Mills, *J. Am. Chem. Soc.*, 2017, **139**, 18714–18724.
59 S. Jiang, S. Liu, L. Zhou, B. Wang, Z. Wang and S. Gao, *Inorg. Chem.*, 2012, **51**, 3079–3087.
60 F. Pointillart, O. Cador, B. Le Guennic and L. Ouahab, *Coord. Chem. Rev.*, 2017, **346**, 150–175.
61 Y. Guo, G. Xu, Y. Guo and J. Tang, *Dalton Trans.*, 2011, **40**, 9953–9963.
62 L. T. A. Ho and L. F. Chibotaru, *Phys. Rev. B: Condens. Matter Mater. Phys.*, 2016, **94**, 104422.
63 S. T. Liddle and J. van Slageren, *Chem. Soc. Rev.*, 2015, **44**, 6655–6669.
64 K. S. Pedersen, J. Dreiser, H. Weihe, R. Sibille, H. V. Johannesen, M. A. Sørensen, B. E. Nielsen, M. Sigrist, H. Mutka, S. Rols, J. Bendix and S. Piligkos, *Inorg. Chem.*, 2015, **54**, 7600–7606.
65 I. F. Galván, M. Vacher, A. Alavi, C. Angeli, F. Aquilante, J. Autschbach, J. J. Bao, S. I. Bokarev, N. A. Bogdanov, R. K. Carlson, *et al.*, OpenMolcas: From Source Code to Insight, *J. Chem. Theory Comput.*, 2019, **15**(11), 5925–5964.
66 L. Ungur, M. Thewissen, J. P. Costes, W. Wernsdorfer and L. F. Chibotaru, *Inorg. Chem.*, 2013, **52**, 6328–6337.
67 J. J. Bishop, A. Davison, M. L. Katcher, D. W. Lichtenberg, R. E. Merrill and J. C. Smart, *J. Organomet. Chem.*, 1971, **27**, 241–249.
68 G. A. Bain and J. F. Berry, *J. Chem. Educ.*, 2008, **85**, 532–536.